Supplementary Information for "The overall-subshear and multi-segment rupture of the 2023 Mw7.8 Kahramanmaraş, Turkey earthquake in millennia supercycle"

Liuwei Xu[1], Saeed Mohanna[1], Lingsen Meng[1,*], Chen Ji[2,*], Jean-Paul Ampuero[3], Zhang Yunjun[4], Masooma Hasnain[1], Risheng Chu[5], Cunren Liang[6]

[1]Department of Earth, Planetary and Space Sciences, University of California Los Angeles, Los Angeles, CA, USA.
[2]Department of Earth Science, University of California Santa Barbara, Santa Barbara, CA, USA.
[3]Observatoire de la Côte d'Azur, Université Côte d'Azur, IRD, CNRS, Valbonne, France.
[4]National Key Laboratory of Microwave Imaging Technology, Aerospace Information Research Institute, Chinese Academy of Sciences, Beijing, China.
[5]State Key Laboratory of Geodesy and Earth's Dynamics, Innovation Academy for Precision Measurement Science and Technology, Chinese Academy of Sciences, Wuhan, China
[6]Institute of Remote Sensing and Geographical Information System, School of Earth and Space Sciences, Peking University, Beijing, China

*Corresponding authors: Lingsen Meng (lsmeng@g.ucla.edu); Chen Ji (ji@geol.ucsb.edu)

Contents of this file

Supplementary Tables 1. The coordinates of the aftershocks used to calibrate the BP results. The time and coordinates of the aftershocks from the AFAD catalog are shown on the left. The results of the aftershock locations before and after slowness calibration are shown along with their distance errors and root-mean-square error relative to the location in the AFAD catalog. (a) shows the results of the AK array BP of the Mw 7.8 event, (b) shows the results of the CH array BP of the Mw 7.8 event, (c) shows the results of the AK array BP of the Mw 7.5 event, and (d) shows the results of the CH array BP of the Mw 7.5 event.

(a)

AFAD			BP results (AK Mw 7.8)					
			Before calibration			After calibration		
time	longitude	latitude	longitude	latitude	Distance error (km)	longitude	latitude	Distance error (km)
2023-02-06T20:37:51	37.05	37.30	36.86	37.18	21.49	37.02	37.31	2.88
2023-02-07T03:13:12	37.66	37.81	37.59	37.55	29.51	37.63	37.75	7.16
2023-02-06T01:51:21	36.59	36.88	36.54	36.87	4.59	36.74	36.94	14.93
2023-02-06T05:36:32	36.14	36.34	35.90	36.26	23.31	36.06	36.34	7.18
2023-02-06T01:46:26	38.05	38.07	38.19	37.99	15.16	38.11	38.15	10.32
2023-02-06T02:03:36	37.88	37.91	37.95	37.71	23.04	37.91	37.87	5.16
2023-02-06T06:54:57	37.46	37.73	37.26	37.59	23.51	37.42	37.71	4.18
RMS error (km):					**21.42**			**8.32**

(b)

AFAD			BP results (CH Mw 7.8)					
			Before calibration			After calibration		
time	longitude	latitude	longitude	latitude	Distance error (km)	longitude	latitude	Distance error (km)
2023-02-06T20:37:51	37.05	37.30	37.1	37.19	12.99	37.1	37.31	4.57
2023-02-07T03:13:12	37.66	37.81	37.55	37.59	26.27	37.59	37.71	12.70
2023-02-06T10:51:28	38.19	38.31	38.07	38.19	16.96	38.19	38.32	1.11
2023-02-06T01:51:21	36.59	36.88	36.5	36.75	16.51	36.58	36.86	2.39
2023-02-06T16:32:11	36.39	36.70	36.42	36.62	9.27	36.41	36.74	4.79
2023-02-09T07:18:17	36.65	37.07	36.69	36.99	9.57	36.69	37.1	4.87

2023-02-06T02:01:45	36.99	37.29	36.9	37.19	13.67	36.94	37.27	4.96
2023-02-06T05:36:32	36.14	36.34	36.13	36.22	13.35	36.13	36.34	0.90
2023-02-06T04:16:49	37.26	37.50	37.22	37.35	17.02	37.27	37.47	3.45
2023-02-06T02:03:36	37.88	37.91	37.87	37.83	8.92	37.91	37.91	2.64
2023-02-06T06:54:57	37.46	37.73	37.43	37.55	20.15	37.47	37.67	6.72
RMS error (km):					**15.78**			**5.44**

(c)

AFAD			BP results (AK Mw 7.5)					
			Before calibration			After calibration		
time	longitude	latitude	longitude	latitude	Distance error (km)	longitude	latitude	Distance error (km)
2023-02-06T12:02:11	36.48	38.07	36.65	38.07	14.92	36.49	38.07	0.88
2023-02-06T21:57:43	36.54	38.06	36.69	38.03	13.58	36.53	38.07	1.41
2023-02-06T17:26:24	36.59	38.12	36.73	38.1	12.48	36.61	38.11	2.08
2023-02-08T14:20:25	37.39	37.99	37.46	37.95	7.59	37.42	37.99	2.64
2023-02-06T13:44:49	37.57	38.01	37.66	37.99	8.21	37.62	37.99	4.92
RMS error (km):					**11.73**			**2.77**

(d)

AFAD			BP results (CH Mw 7.5)					
			Before calibration			After calibration		
time	longitude	latitude	longitude	latitude	Distance error (km)	longitude	latitude	Distance error (km)
2023-02-06T12:02:11	36.48	38.07	36.37	38.07	9.65	36.49	38.07	0.88
2023-02-06T21:57:43	36.54	38.06	36.41	38.03	11.89	36.53	38.07	1.41
2023-02-06T17:26:24	36.59	38.12	36.41	38.07	16.74	36.53	38.11	5.38
2023-02-06T21:15:17	37.07	38.06	36.98	38.03	8.57	37.06	38.07	1.41
2023-02-08T14:20:25	37.39	37.99	37.3	37.94	9.66	37.38	37.95	4.53
2023-02-06T13:44:49	37.57	38.01	37.5	38.02	6.25	37.54	38.03	3.44
RMS error (km):					**10.96**			**3.32**

Supplementary Table 2. Summary of rupture speeds resolved by contemporary studies, sorted by publication or post time. Red color indicates supershear speeds, and green color indicates subshear speeds. V_{NE}: northeast rupture speed; V_{SW}: southwest rupture speed; V_{Narli}: rupture speed on Narli fault. SEBP: Slowness-Enhanced Back-projection. FFI: finite fault inversion. Datasets adopted by FFI are listed (if applicable). The different types of rupture speeds are denoted within parentheses as follows:
Average: the mean speed declared by the studies.
Maximum: the maximum speed declared by the studies.
Near-station: the speed calculated using waveform component analysis at stations near the fault.

	V_{NE}	V_{SW}	V_{Narli}	Method	Data of FFI
Rosakis et al.[1]	/	/	~5.1 km/s (near-station)	Near-field data analysis	/
Melgar et al.[2]	3.2 km/s (FFI, maximum)	3.2 km/s (FFI, maximum)	3.2 km/s (FFI, maximum)	FFI	Local strong motion, GNSS
Okuwaki et al.[3]	Fast migration	6 km/s (average)	2.5 km/s (average)	Potency-density tensor inversion	Teleseismic
Xu et al. (this study)	~3.05 km/s (SEBP, average)	~3.11 km/s (SEBP, average)	~3.05 km/s (SEBP, average)	SEBP, joint FFI	Local strong motion, GNSS, SAR, teleseismic
Yao & Yang[4]	3.19 km/s (average)	3.1-3.4 km/s (average)	/	Near-field data analysis and rupture simulations	/
Delouis et al.[5]	Globally sub-shear, transiently supershear	Globally sub-shear, transiently supershear	2.8-3.0 km/s (FFI, average)	FFI	Local strong motion, GNSS
Abdelmeguid et al.[6]	Supershear	Supershear and subshear	Subshear and supershear	Near-field data analysis and rupture simulation	/
Mai et al.[7]	3.1 km/s (BP, average)	2 km/s (BP, average)	2.5 km/s (BP, average)	BP, FFI	Teleseismic, SAR

Petersen et al.[8]	1.8 km/s (BP, average) 3.4 km/s (BP, maximum) 2.6 ± 0.4 km/s (FFI, average)	1.8 km/s (BP, average) 3.4 km/s (BP, maximum) 2.6 ± 0.4 km/s (FFI, average)	1.8 km/s (BP, average) 3.4 km/s (BP, maximum) 2.6 ± 0.4 km/s (FFI, average)	BP, finite source inversion	Teleseismic, local strong motion
Wang et al.[9]	Supershear	Supershear and subshear	Supershear	Rupture simulation	/

Supplementary Table 3. The information of the M5.3 aftershock used for Mach wave search.

Time (UTC)	Latitude	Longitude	Magnitude (Mw)
2023-02-06 20:37:51	37.2588° N	37.1017° E	5.3

Supplementary Table 4. A summary of fault parameters on the four segments of EAF. Long-term slip rates are from Duman and Emre[10]. Lengths (L) are determined based on our FFI fault plane lengths and fault maps in Duman and Emre[10]. Rigidity and G-R law constants are from Güvercin et al.[11]. The seismogenic depth is determined according to our coseismic model and the seismicity distribution in Güvercin et al.[11].

Fault Segment	Erkenek	Pazarcık	Amanos
Long-term fault slip rates (mm/yr)	7	7	3
Length (L, km)	60	121	131
a value in G-R law	3.2	3.9	3.8
b value in G-R law, since largest reported earthquake	0.88	0.94	0.92
b value in G-R law, 2007-2019	1.3	1.1	1.1
Corresponding FFI fault planes (Figure 1b)	S3	S2, S4, East part of S5	S6, west part of S5
Rigidity (μ, GPa)	29		
Seismogenic depth (H, km)	20		

Supplementary Table 5. The significant historical events included in the moment history calculation (Ambraseys & Jackson[12]; Palutoglu & Sasmaz[13]).

Time	Longitude	Latitude	Magnitude	Reference
1114	37.5	37.5	7.8	Ambraseys & Jackson, 1998
1795	37.3	37.6	7	Palutoglu & Sasmaz, 2017
1822	36.5	36.7	7.5	Ambraseys & Jackson, 1998
1872	36.4	36.4	7.2	Ambraseys & Jackson, 1998
1893	38.3	38.0	7.1	Ambraseys & Jackson, 1998

Supplementary Table 6. Historical large (M>=6.5) earthquakes in south California (USGS, ANSS catalog).

Event index in Figure 5b	Time (YYYY, MM, DD)	Longitude	Latitude	Magnitude
1	2019, 7, 6	-117.599	35.769	7.1
2	1999, 10, 16	-116.265	34.603	7.1
3	1994, 1, 17	-118.537	34.213	6.7
4	1992, 6, 28	-116.437	34.2	7.3
5	1987, 11, 24	-115.852	33.015	6.6
6	1971, 2, 9	-118.37	34.416	6.6
7	1968, 4, 9	-116.103	33.179	6.6
8	1952, 7, 21	-118.998	34.958	7.5
9	1947, 4, 10	-116.531	34.982	6.5
10	1942, 10, 21	-115.785	32.975	6.6
11	1940, 5, 19	-115.381	32.844	6.9
12	1927, 11, 4	-120.705	34.68	6.9
13	1925, 6, 29	-119.8	34.3	6.8
14	1922, 3, 10	-119.143	34.209	6.5
15	1918, 4, 21	-116.972	33.762	6.7

16	1899, 12, 25	-117	33.8	6.7
17	1892, 5, 28	-116.2	33.2	6.5
18	1890, 2, 9	-116.3	33.4	6.75
19	1857, 1, 9	-120.3	35.7	7.93
20	1812, 12, 21	-119.9	34.2	7.1
21	1812, 12, 8	-117.65	34.37	7.5

Supplementary Table 7. Synthetic Aperture Radar (SAR) image pairs analyzed.

Sensor (band)	Mode	Pass	Track (Frame)	Preseismic Date	Postseismic Date	Acquisition Time UTC (local time)	Analyze Method
Sentinel-1A (C-band)	TOPS	Asc	014 (N/A)	2023-01-28	2023-02-09	15:34 (18:34)	Speckle tracking
	TOPS	Asc	116 (N/A)	2023-02-04	2023-02-28	15:26 (18:26)	Speckle tracking
	TOPS	Dsc	021 (N/A)	2023-01-29	2023-02-10	03:34 (06:34)	Speckle tracking
ALOS-2 (L-band)	ScanSAR	Asc	184 (700-750)	2022-09-05	2023-02-20	21:28 (00:28)	InSAR + MAI
	ScanSAR	Dsc	077 (2850-2900)	2022-09-16	2023-02-17	09:33 (12:33)	InSAR + MAI
LuTan-1A/B (L-band)	Stripmap	Dsc	068 (N/A)	2022-04-11	2023-02-10	03:34 (06:34)	InSAR

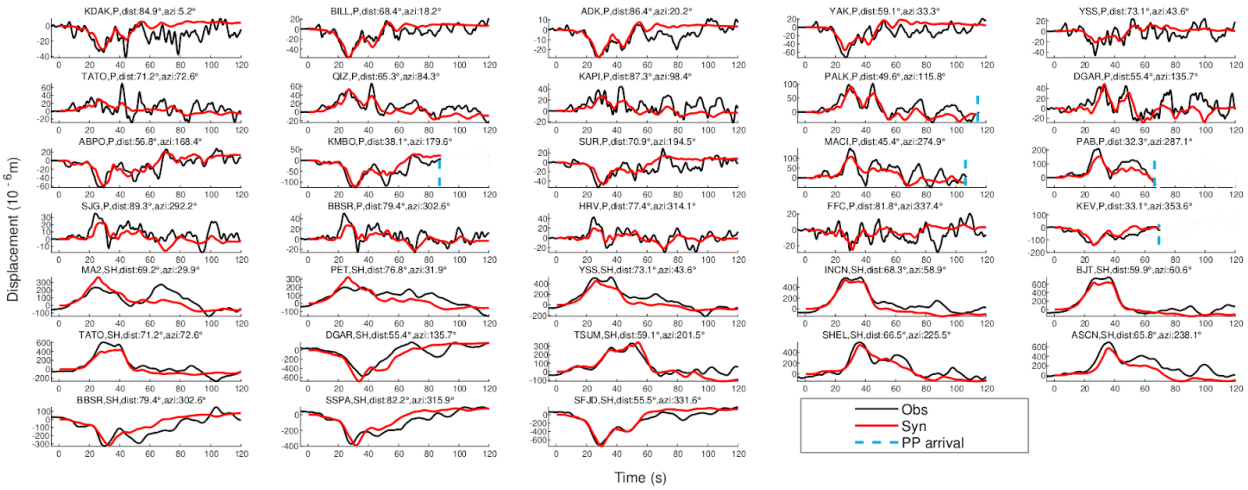

Supplementary Figure 1. Comparison between observed teleseismic broadband body wave waveforms (black lines) and synthetic seismograms (red lines) generated by the preferred model of the Mw 7.8 event. The wave type and the station name are shown at the top of each trace, along with azimuth and epicenter distance in degree. The vertical cyan dash lines denote the PP arrival time.

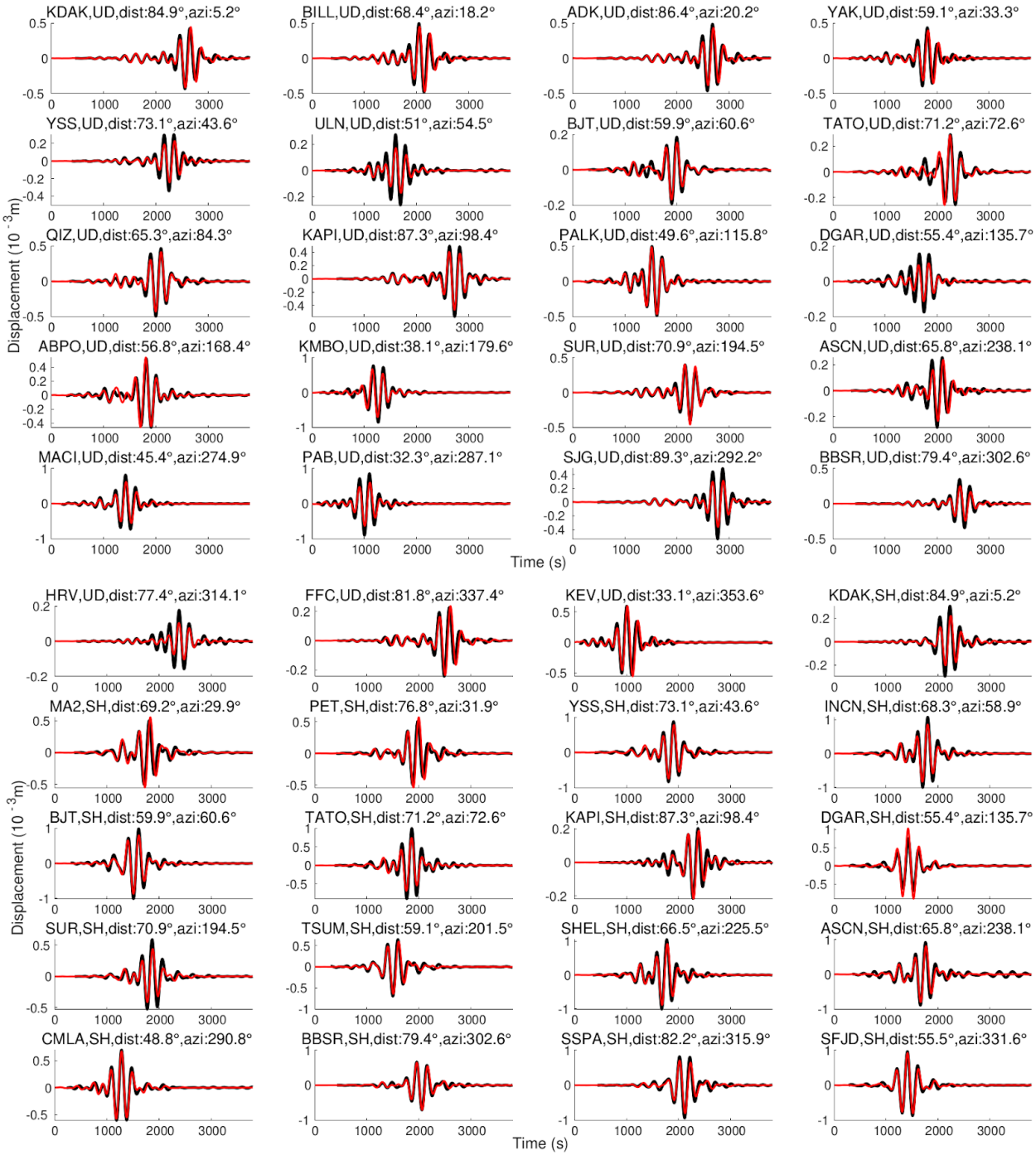

Supplementary Figure 2. Comparison between observed teleseismic long-period surface wave waveforms (black lines) and synthetic seismograms (red lines) generated by the preferred model of the Mw 7.8 event. The wave type and the station name are shown at the top of each trace, along with azimuth and epicenter distance in degree.

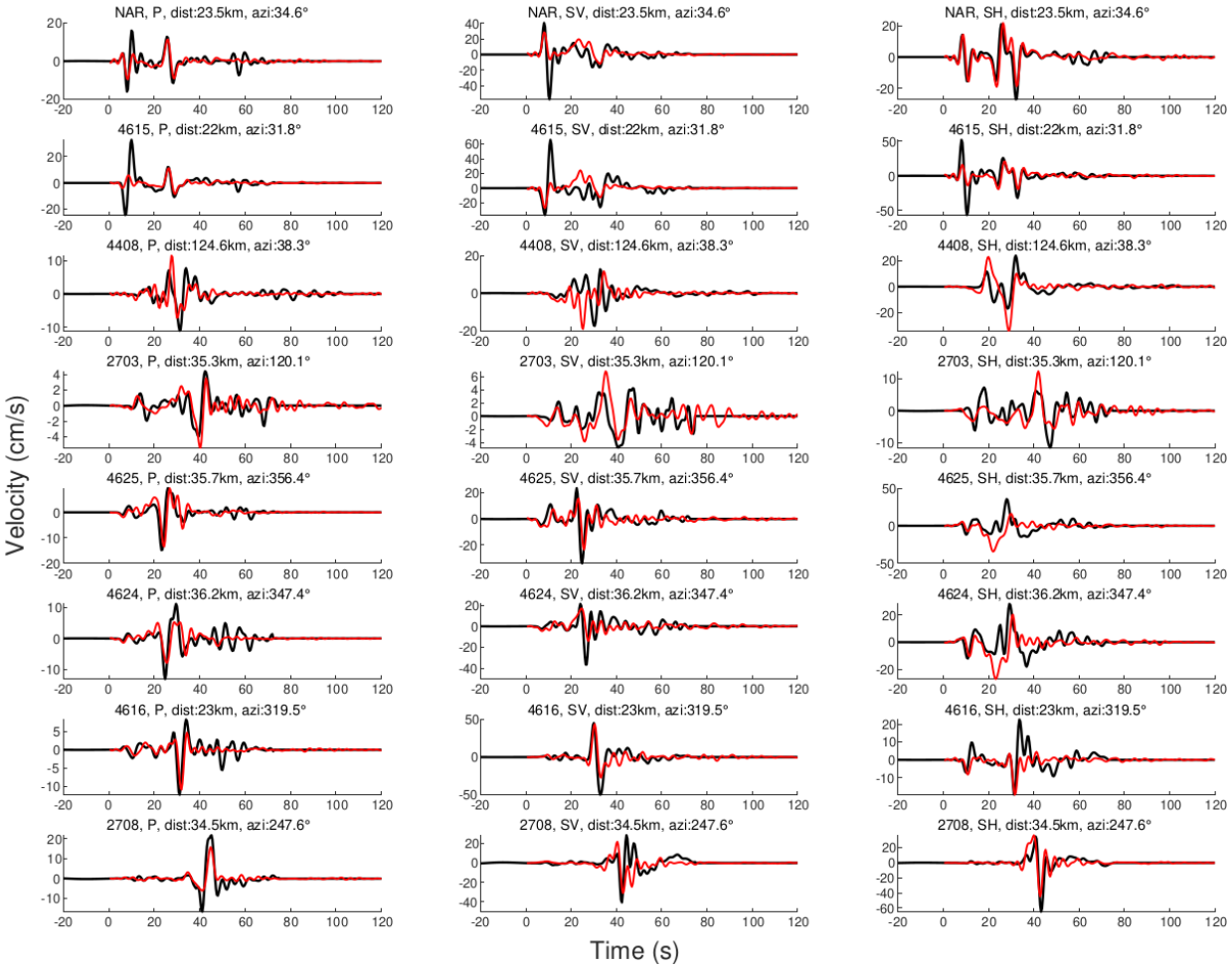
NAR, P, dist:23.5km, azi:34.6°
NAR, SV, dist:23.5km, azi:34.6°
NAR, SH, dist:23.5km, azi:34.6°
4615, P, dist:22km, azi:31.8°
4615, SV, dist:22km, azi:31.8°
4615, SH, dist:22km, azi:31.8°
4408, P, dist:124.6km, azi:38.3°
4408, SV, dist:124.6km, azi:38.3°
4408, SH, dist:124.6km, azi:38.3°
2703, P, dist:35.3km, azi:120.1°
2703, SV, dist:35.3km, azi:120.1°
2703, SH, dist:35.3km, azi:120.1°
4625, P, dist:35.7km, azi:356.4°
4625, SV, dist:35.7km, azi:356.4°
4625, SH, dist:35.7km, azi:356.4°
4624, P, dist:36.2km, azi:347.4°
4624, SV, dist:36.2km, azi:347.4°
4624, SH, dist:36.2km, azi:347.4°
4616, P, dist:23km, azi:319.5°
4616, SV, dist:23km, azi:319.5°
4616, SH, dist:23km, azi:319.5°
2708, P, dist:34.5km, azi:247.6°
2708, SV, dist:34.5km, azi:247.6°
2708, SH, dist:34.5km, azi:247.6°
Velocity (cm/s)
Time (s)

(continue)

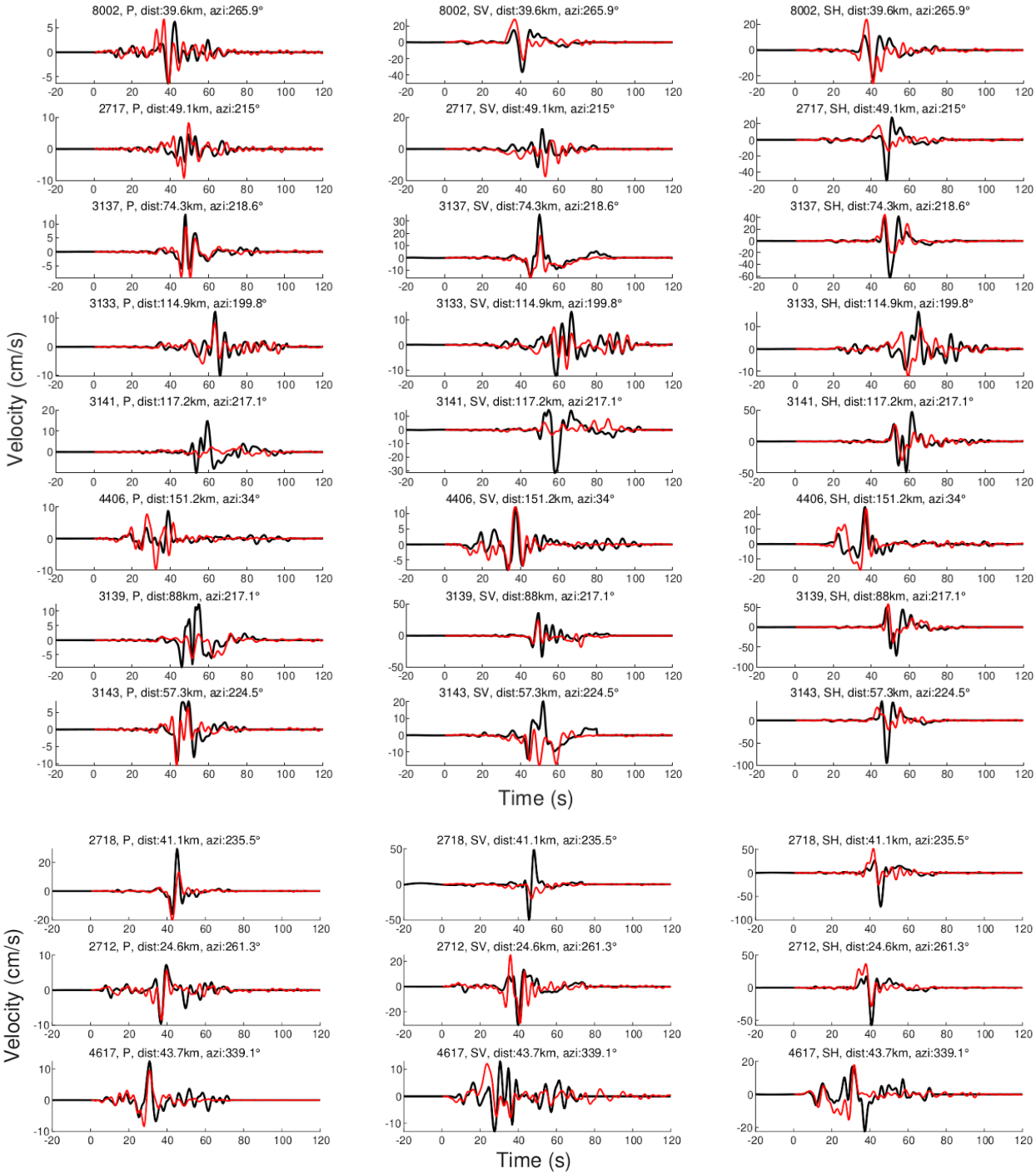

Supplementary Figure 3. Comparison between observed near-field strong motion station waveforms (black lines) and synthetic seismograms (red lines). The component and the station name are shown at the top of each trace, accompanied by azimuth in degree and epicenter distance in km. The unit of velocity waveforms is cm/s.

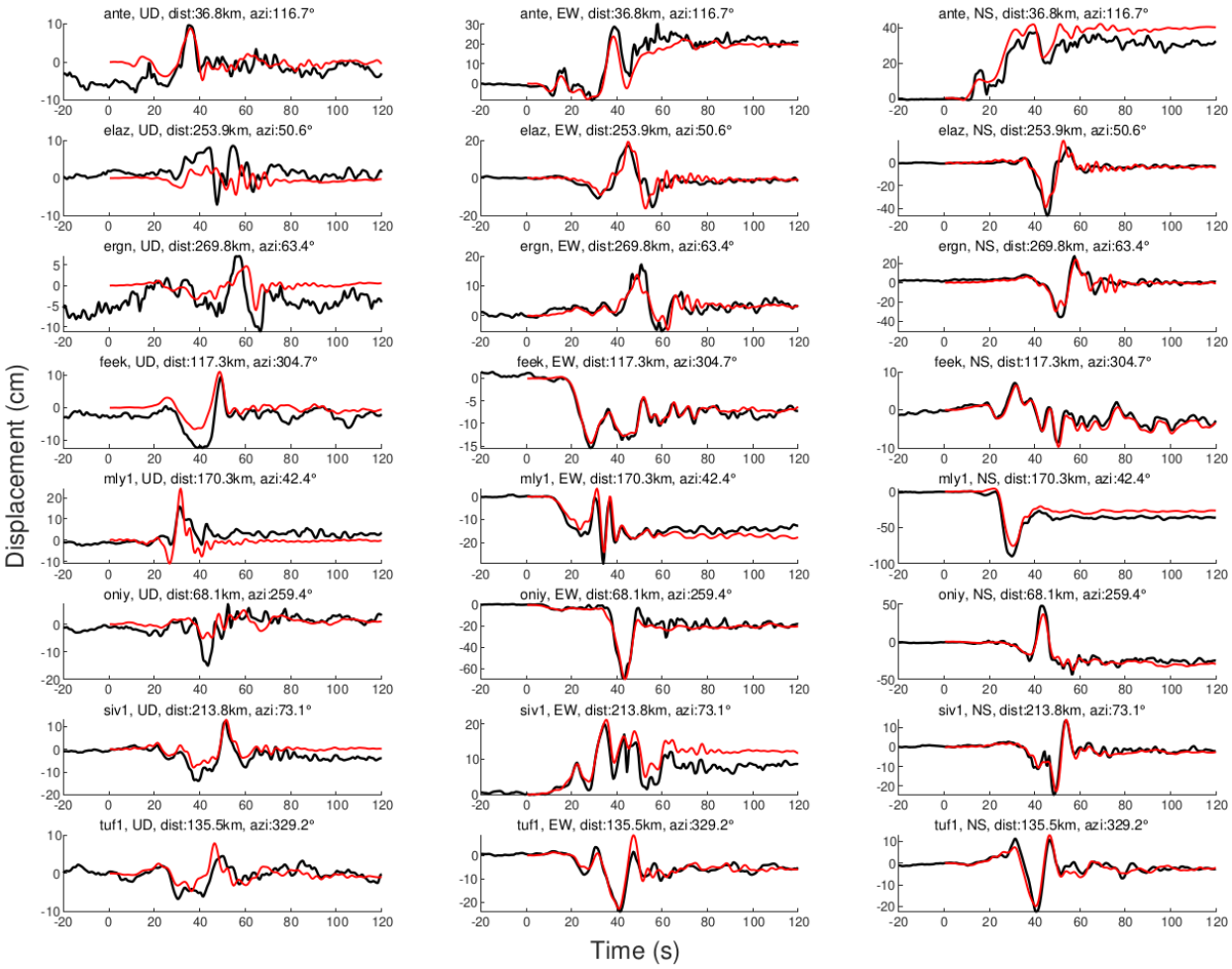

Supplementary Figure 4. Comparison between observed near-field high-rate GNSS waveforms (black lines) and synthetic seismograms (red lines). The component and the station name are shown at the top of each trace, accompanied by azimuth in degree and epicenter distance in km. The unit of displacement waveforms is cm.

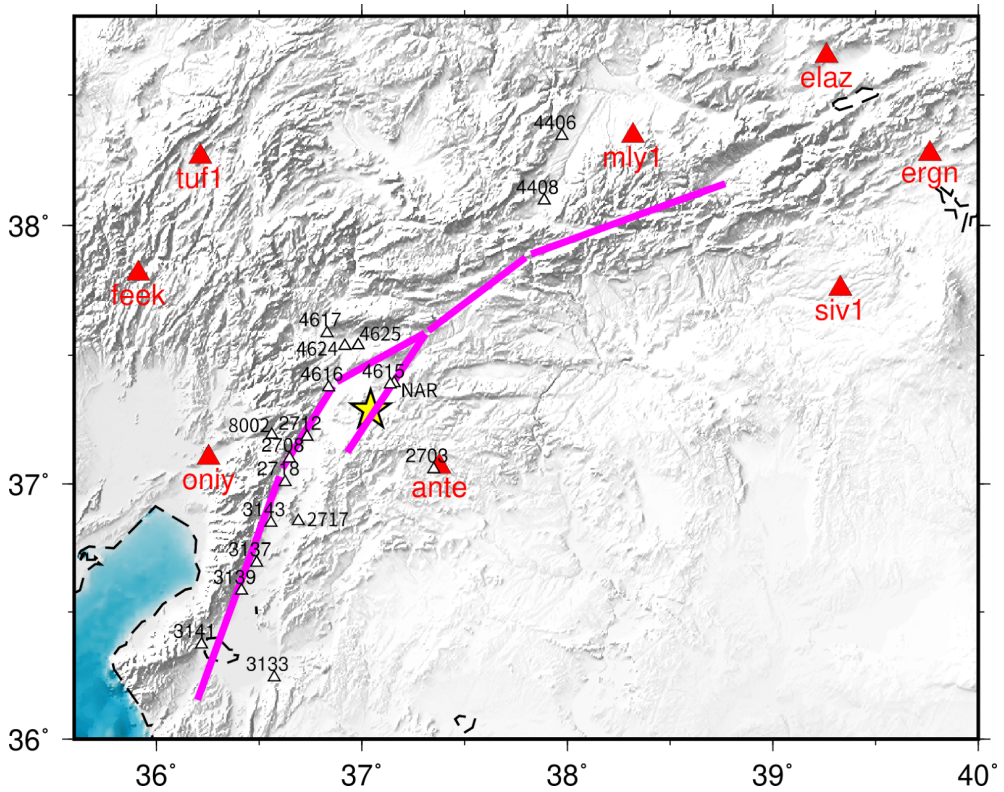

Supplementary Figure 5. The map showing the strong motion (white triangles) and high-rate GNSS (red triangles) stations used in this study, with corresponding names. Thick magenta line denotes the surface trace of the fault model.

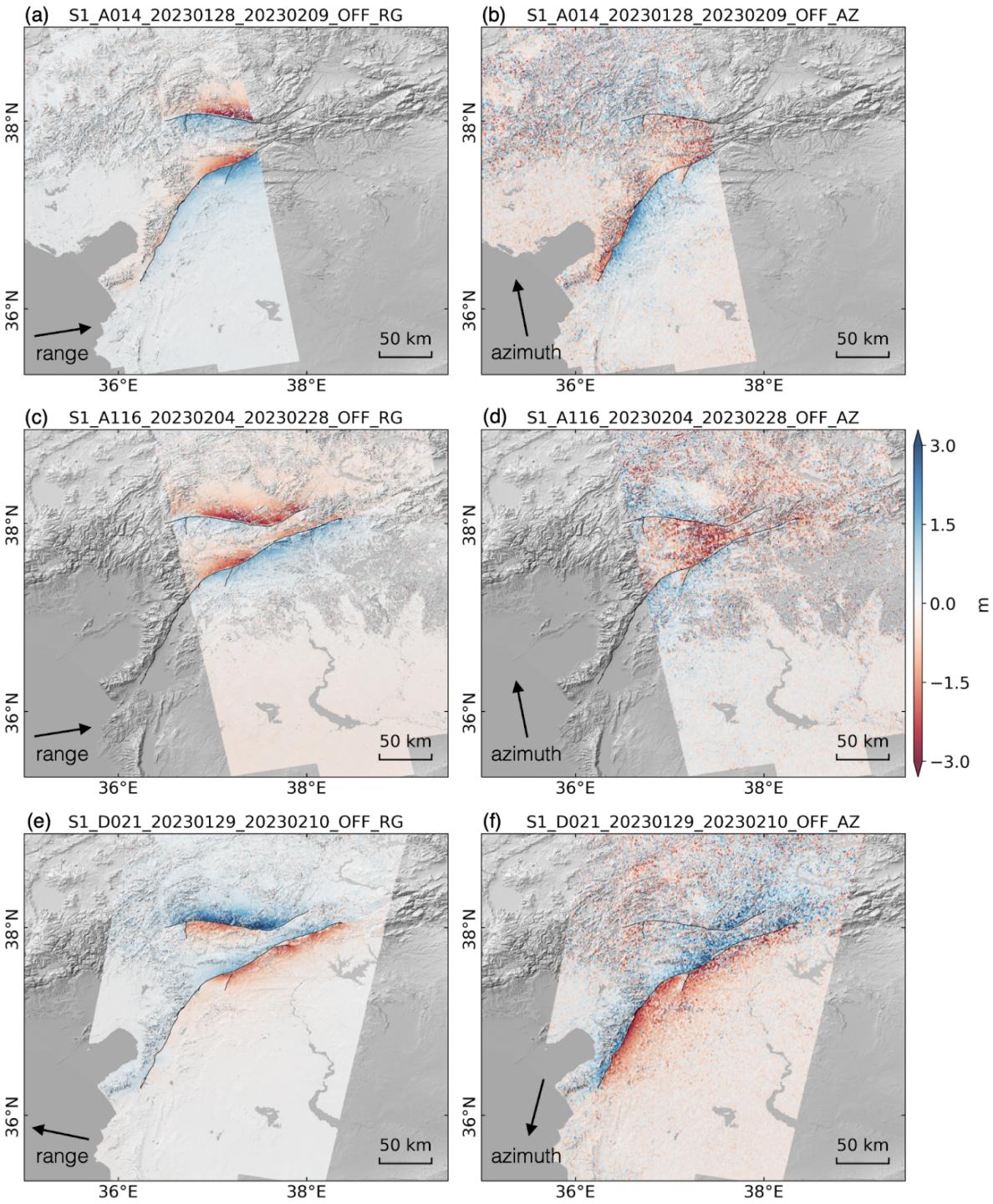
(a) S1_A014_20230128_20230209_OFF_RG
(b) S1_A014_20230128_20230209_OFF_AZ
(c) S1_A116_20230204_20230228_OFF_RG
(d) S1_A116_20230204_20230228_OFF_AZ
(e) S1_D021_20230129_20230210_OFF_RG
(f) S1_D021_20230129_20230210_OFF_AZ
38°N
36°N
36°E
38°E
range
azimuth
50 km
3.0
1.5
0.0
−1.5
−3.0
m

(continue)

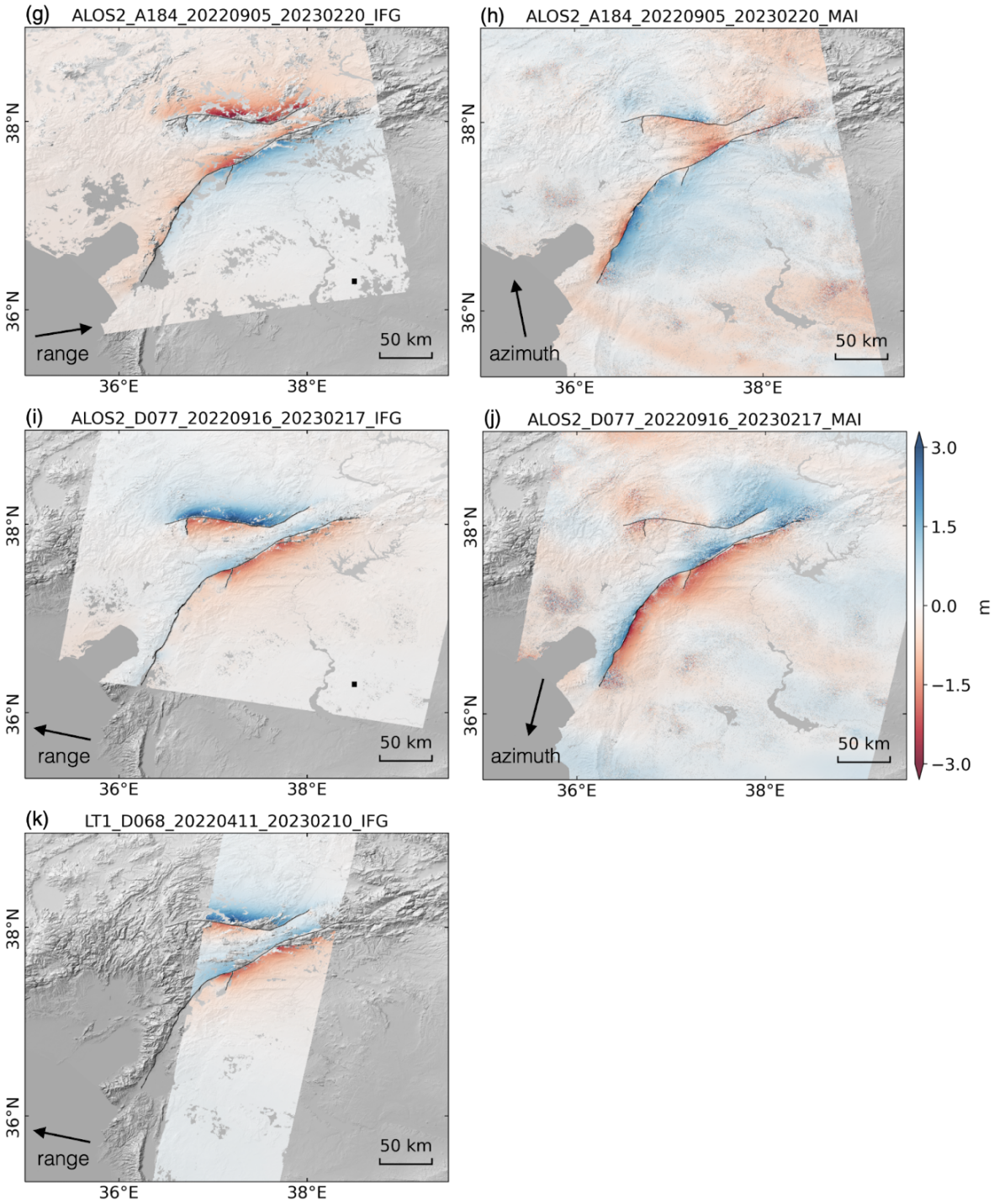

Supplementary Figure 6. The original resolution displacement data. (a-b) Sentinel-1 ascending track 014 offset in range and azimuth directions, respectively. (c-d) Same as (a-b) but for Sentinel-1 ascending track 116. (e-f) Same as (a-b) but for Sentinel-1 descending track 021. (g-h) ALOS-2 ascending track 184 InSAR and MAI displacement in range and azimuth directions, respectively. (i-j) Same as (g-h) but for ALOS-2 descending track 077. (k) LuTan-1 descending track 068 InSAR displacement in range direction.

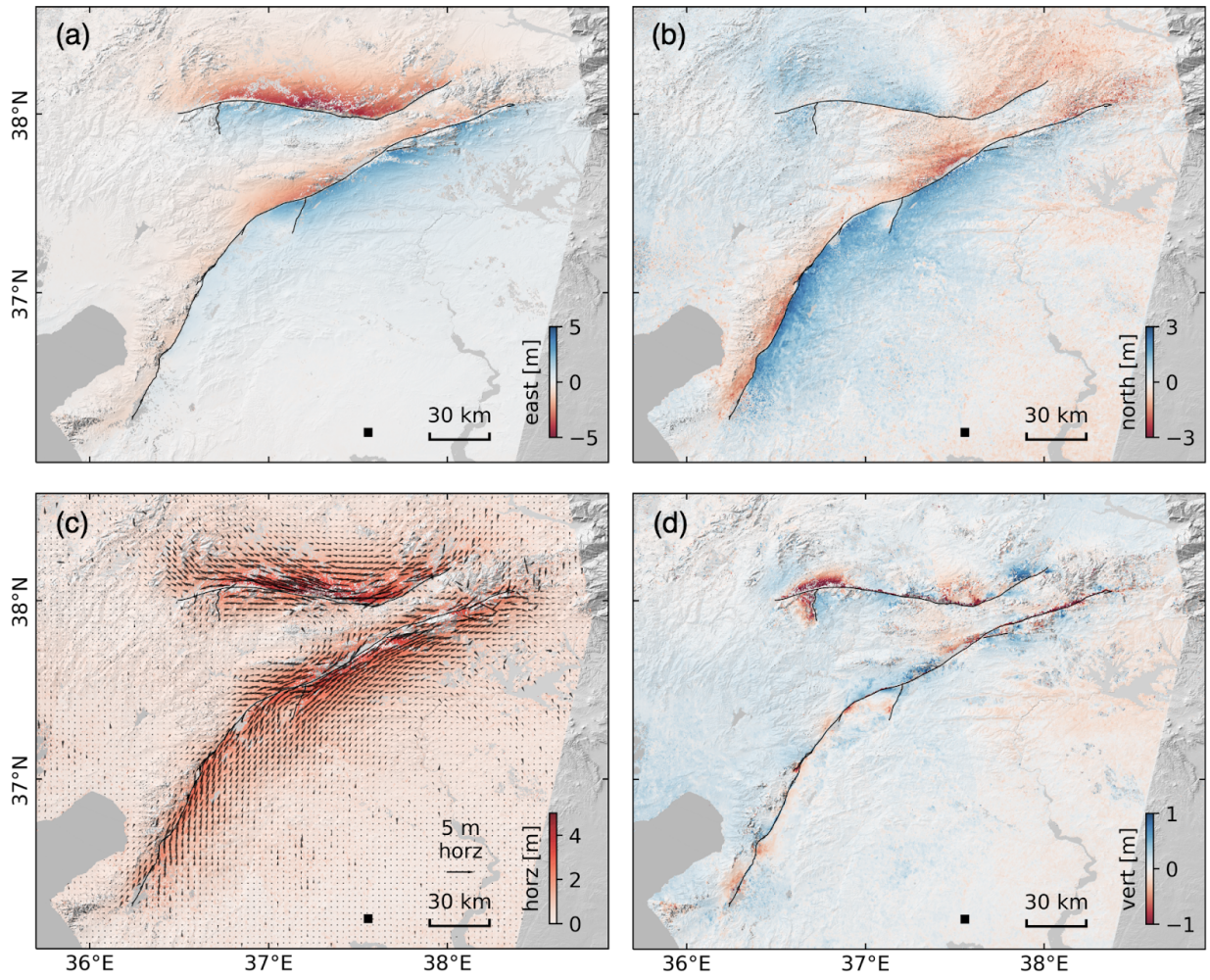

Supplementary Figure 7. 3D deformation map for the source region. (a-b) Deformation in the east-west and north-south directions, respectively. (c) Deformation in the horizontal direction with color representing magnitude and arrows representing magnitude and directions. (d) Deformation in the up-down direction. Black square: reference point.

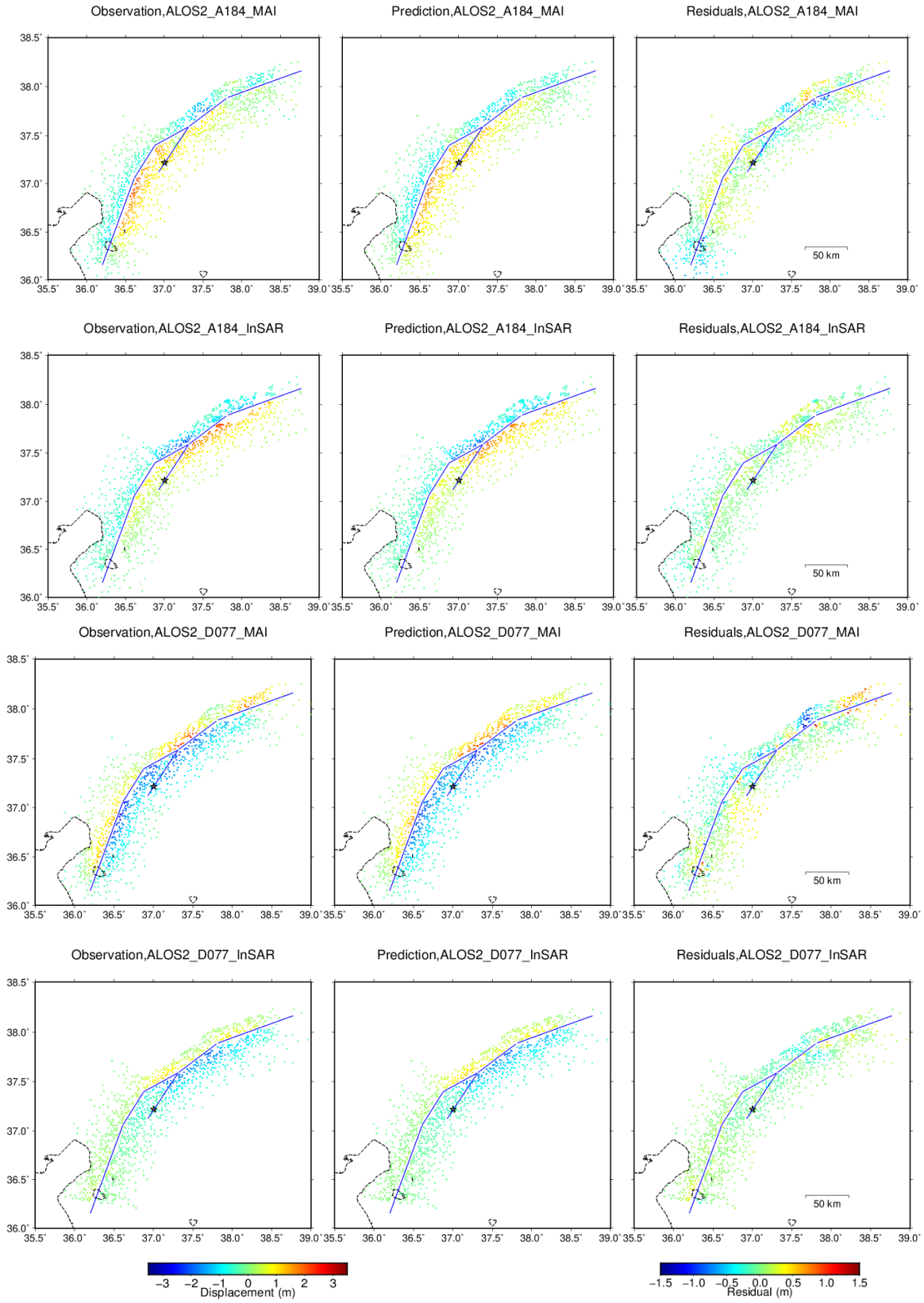
Observation,ALOS2_A184_MAI
Prediction,ALOS2_A184_MAI
Residuals,ALOS2_A184_MAI
Observation,ALOS2_A184_InSAR
Prediction,ALOS2_A184_InSAR
Residuals,ALOS2_A184_InSAR
Observation,ALOS2_D077_MAI
Prediction,ALOS2_D077_MAI
Residuals,ALOS2_D077_MAI
Observation,ALOS2_D077_InSAR
Prediction,ALOS2_D077_InSAR
Residuals,ALOS2_D077_InSAR
50 km
Displacement (m)
Residual (m)

(continue)

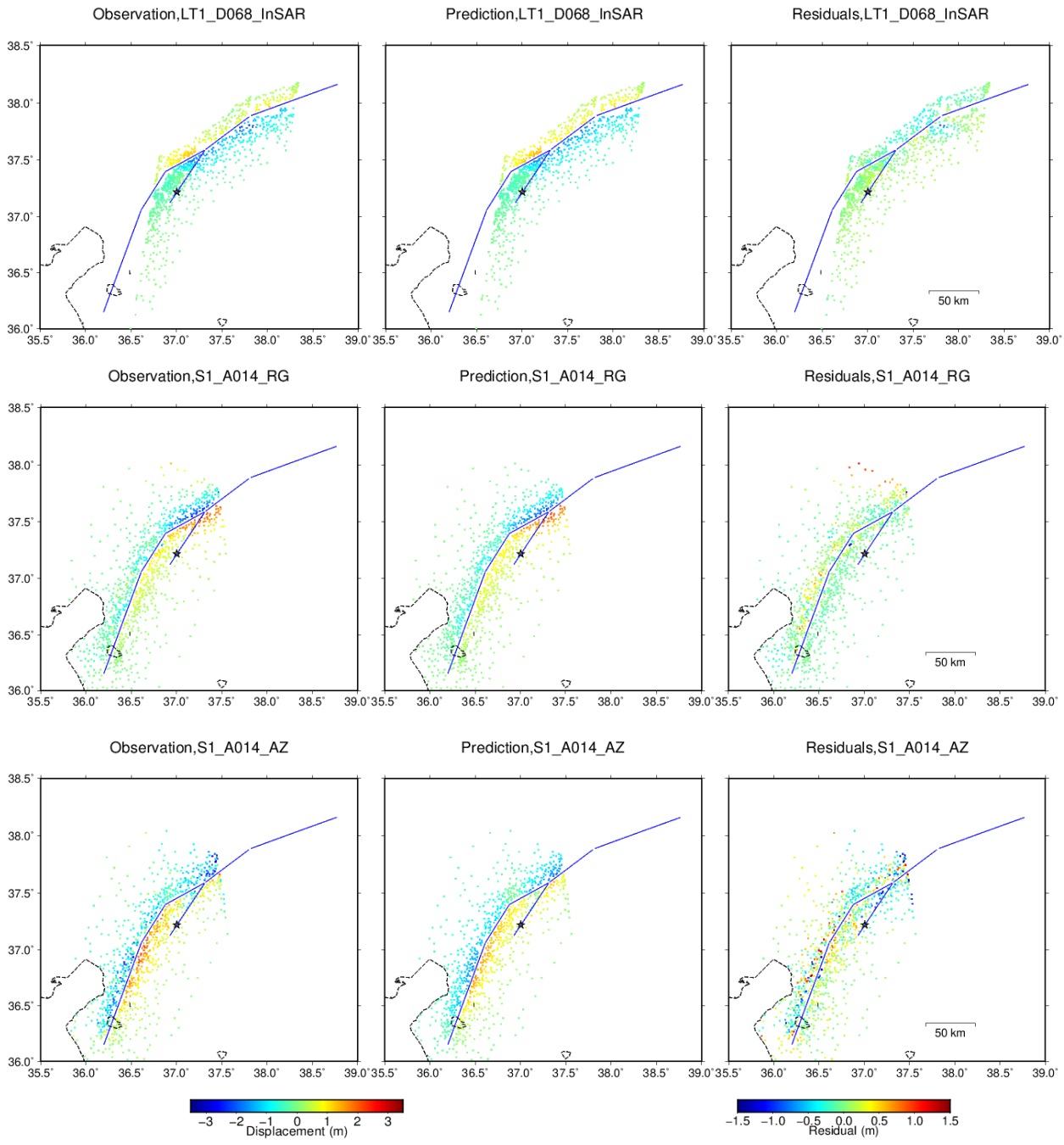
Observation,LT1_D068_InSAR
Prediction,LT1_D068_InSAR
Residuals,LT1_D068_InSAR
Observation,S1_A014_RG
Prediction,S1_A014_RG
Residuals,S1_A014_RG
Observation,S1_A014_AZ
Prediction,S1_A014_AZ
Residuals,S1_A014_AZ
50 km
Displacement (m)
Residual (m)

(continue)

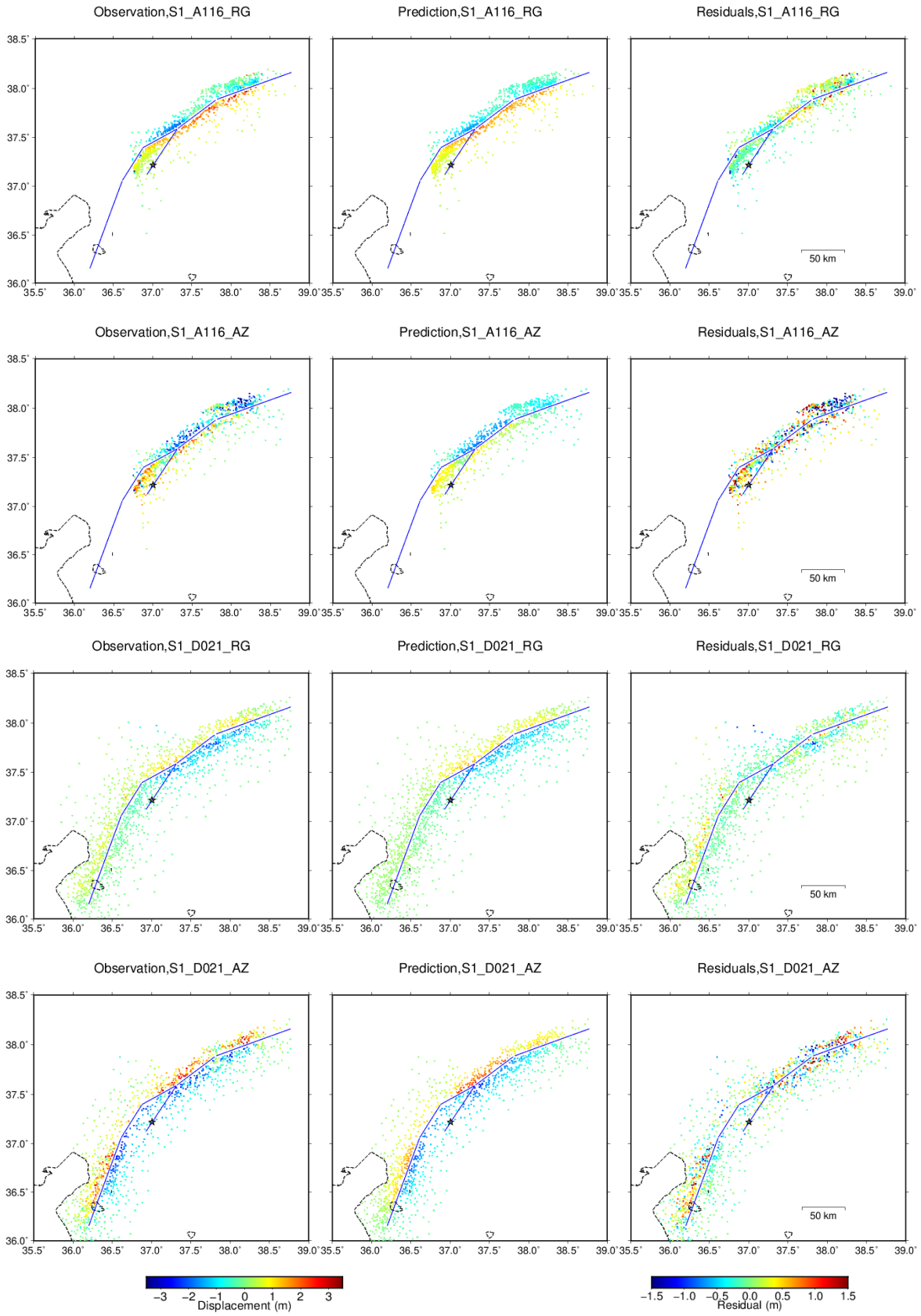
Observation,S1_A116_RG
Prediction,S1_A116_RG
Residuals,S1_A116_RG
Observation,S1_A116_AZ
Prediction,S1_A116_AZ
Residuals,S1_A116_AZ
Observation,S1_D021_RG
Prediction,S1_D021_RG
Residuals,S1_D021_RG
Observation,S1_D021_AZ
Prediction,S1_D021_AZ
Residuals,S1_D021_AZ
50 km
Displacement (m)
Residual (m)

Supplementary Figure 8. The sub-sampled static displacement data fits. The first column is the resampled static displacement (observation). The second column is the prediction by the preferred model. The third column is the residuals obtained by deducting the prediction from the observation.

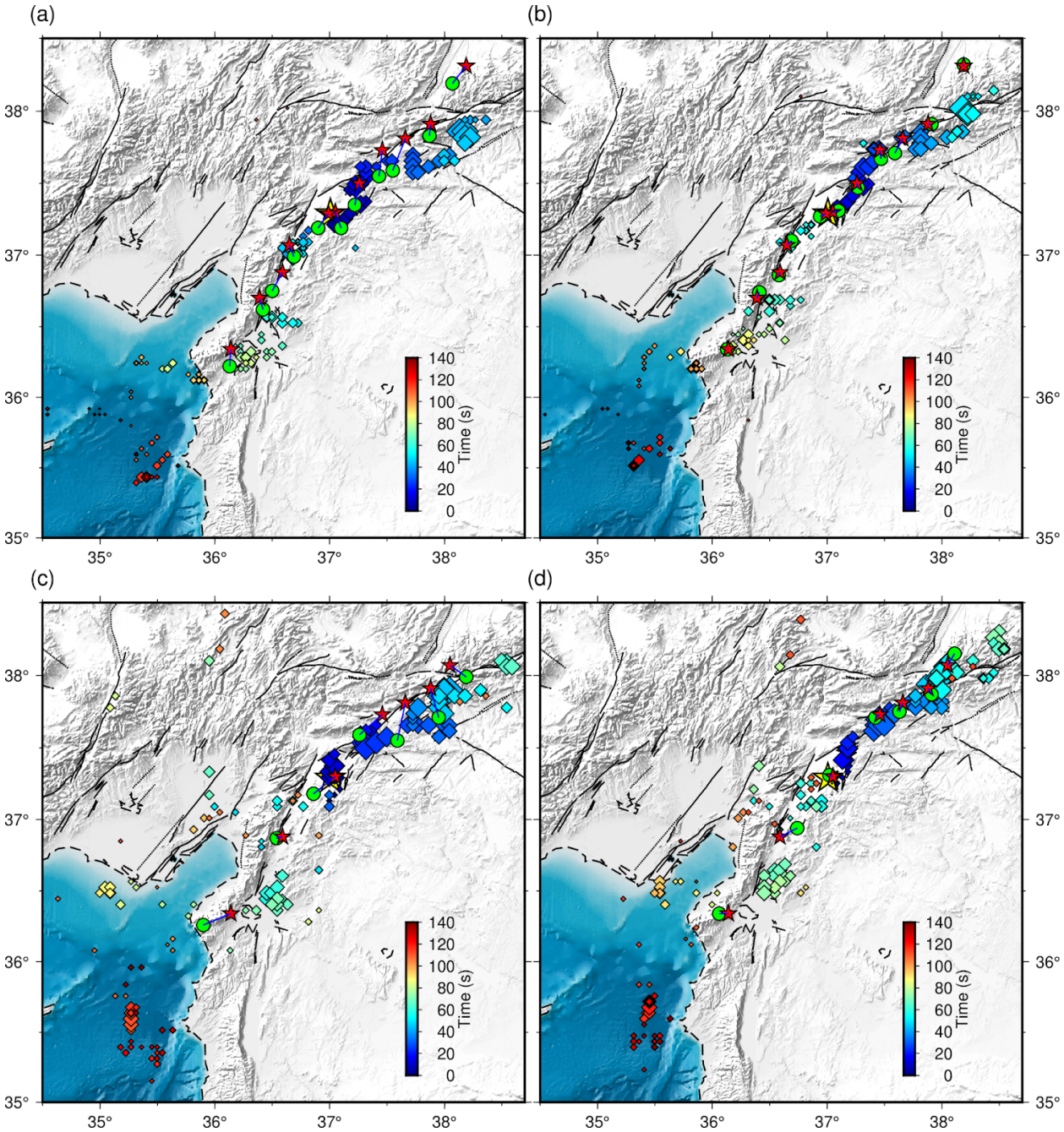

Supplementary Figure 9. Comparison of aftershock locations and mainshock BPs (the Mw 7.8 event) before and after calibration. (a) The CH array's results before slowness calibration. (b) The CH array's results after slowness calibration. (c) The AK array's results before slowness

calibration. (d) The AK array's results after slowness calibration. Green circles denote the BP-inferred locations of M 4.7+ aftershocks spanning the rupture region. The red stars denote the AFAD catalog of aftershocks. The yellow star denotes the epicenter of the mainshock. Diamonds denote the High-Freq radiators for the Mw 7.8 event, color-coded by rupture time relative to the origin time of the event and with a size proportional to the normalized BP power.

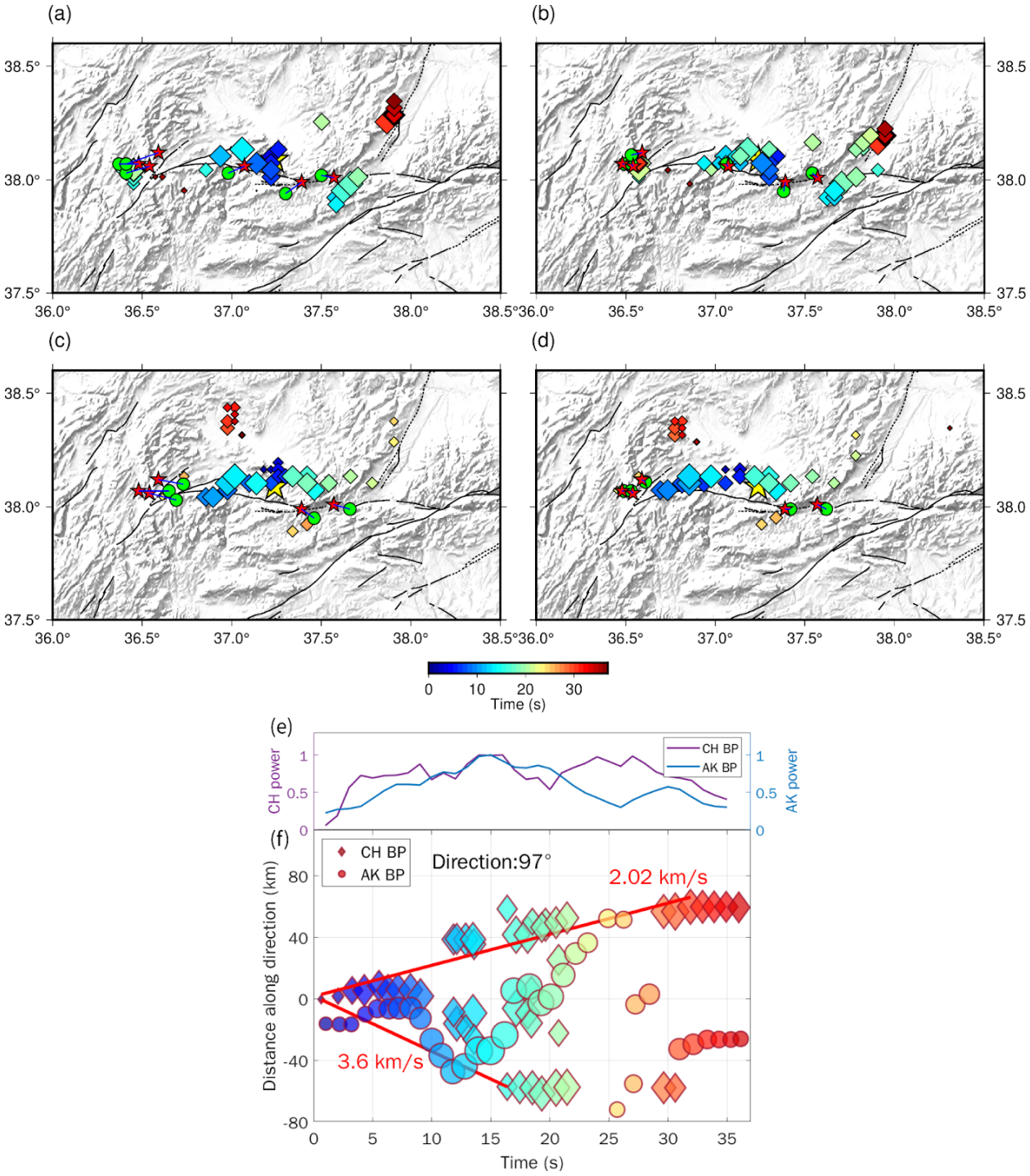

Supplementary Figure 10. Comparison of aftershock locations and mainshock BPs (the Mw 7.5 event) before and after calibration. (a) The CH array's results before slowness calibration. (b) The CH array's results after slowness calibration. (c) The AK array's results before slowness calibration. (d) The AK array's results after slowness calibration. Green circles denote the BP-inferred locations of M 4.7+ aftershocks spanning the rupture region. The red stars denote the AFAD catalog of aftershocks. The yellow star denotes the epicenter of the mainshock. Diamonds denote the High-Freq radiators for the Mw 7.5 event, color-coded by rupture time relative to the origin time of the event and with a size proportional to the normalized BP power. (e) The BP power. The blue and purple curves denote the normalized BP power of AK and CH arrays, respectively. (f) The rupture speeds. The circles denote the High-Freq radiators imaged by the AK array, color-coded by rupture time relative to the origin time of the event and with a size proportional to the normalized BP power. The diamonds denote the same as circles but imaged by the CH array. The red slants and numbers show the fitted rupture speeds for the east branch (97°, positive direction) and for the west branch (277°, negative direction).

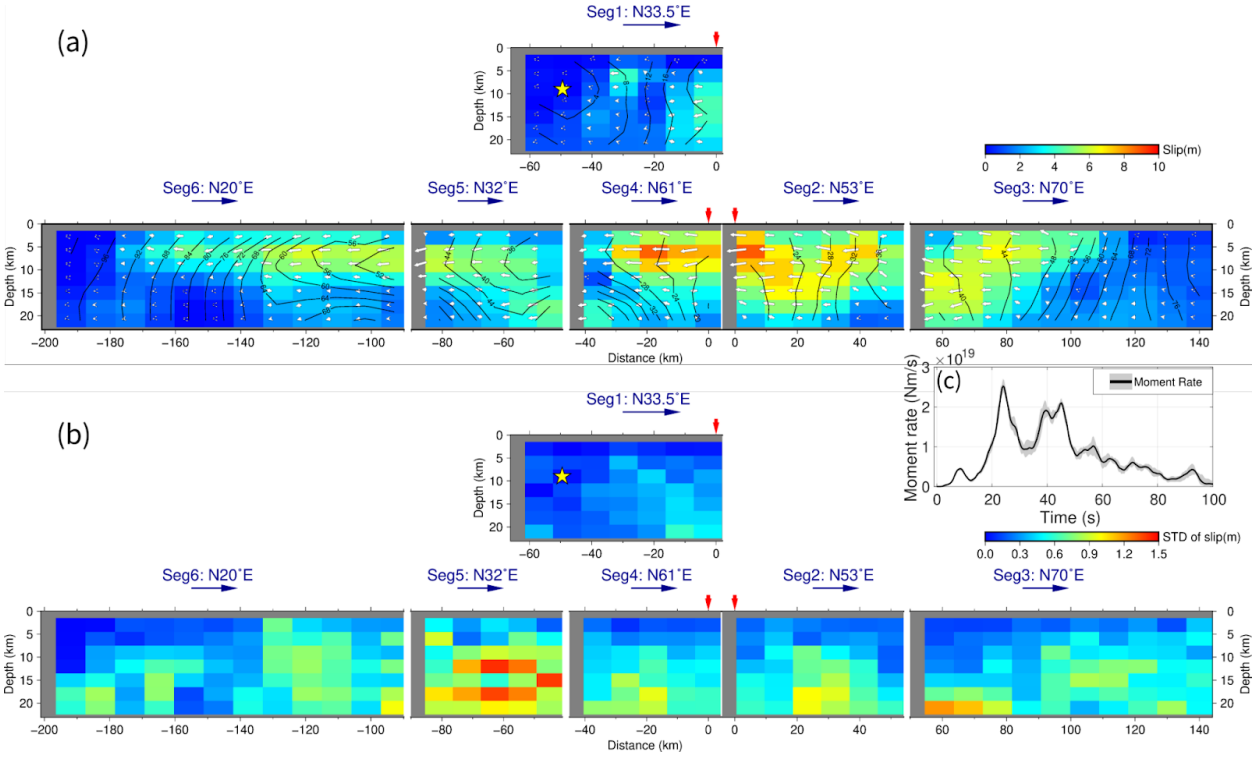

Supplementary Figure 11. Inversion results with ten different random seeds. (a) The average slip model of 10 plausible solutions. The segment index and orientation are shown on the top of each segment. The red arrows indicate the connecting edges of S1, S2, and S4 segments. The black contours denote the slip initiation time. The white arrows indicate the rake angle of each subfault. (b) The standard deviation of the fault slip among the 10 plausible slip models. (c)

Moment rate functions. The black line and the gray area represent the average and the range of moment rates of the 10 plausible models.

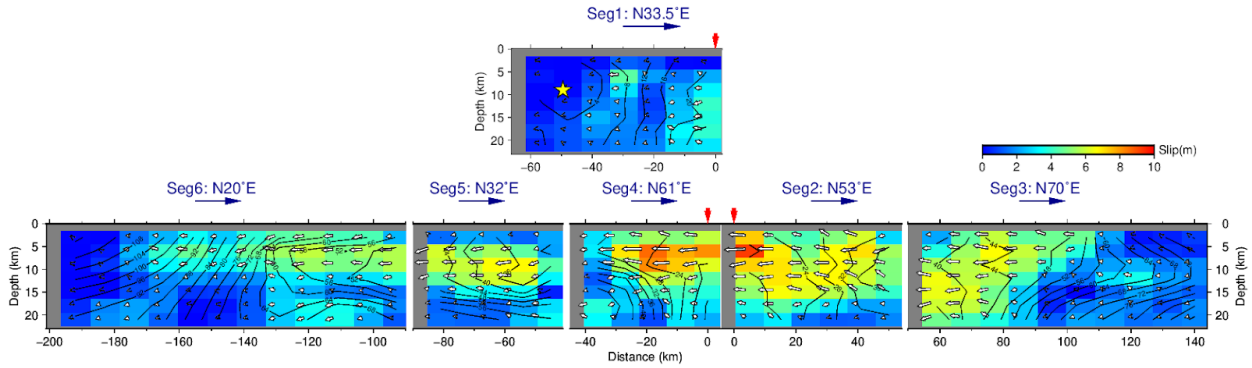

Supplementary Figure 12. The preferred slip model of the Mw 7.8 event in original resolution (9 km along strike, 3 km along depth). The segment index and orientation are shown on the top of each segment. The red arrows indicate the connecting edges of S1, S2, and S4 segments. The black contours denote the slip initiation time. The white arrows indicate the rake angle of each subfault.

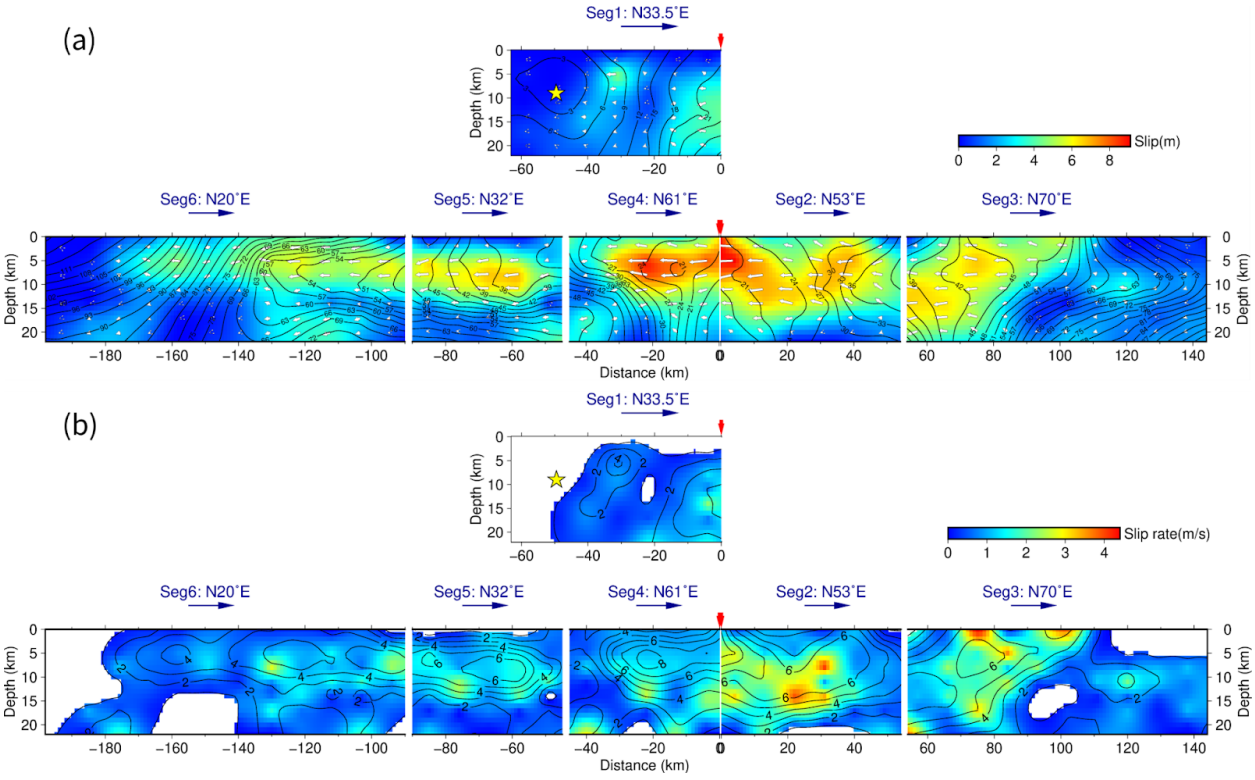

Supplementary Figure 13. The preferred slip model of the Mw 7.8 event. (a) The cross-section view of the slip distribution. The segment index and orientation are shown on the top of each

segment. The red arrows indicate the connecting edges of S1, S2, and S4 segments. The black contours denote the slip initiation time. The white arrows indicate the rake angle of each subfault. (b) The average slip rate defined as the slip amplitude (in meter) over rise time (in second). The black contours denote the slip of the preferred model (in meter). Only sub-sources with slip >= 10% maximum slip are displayed since the rise time for minor slip subfaults is often poorly constrained[9].

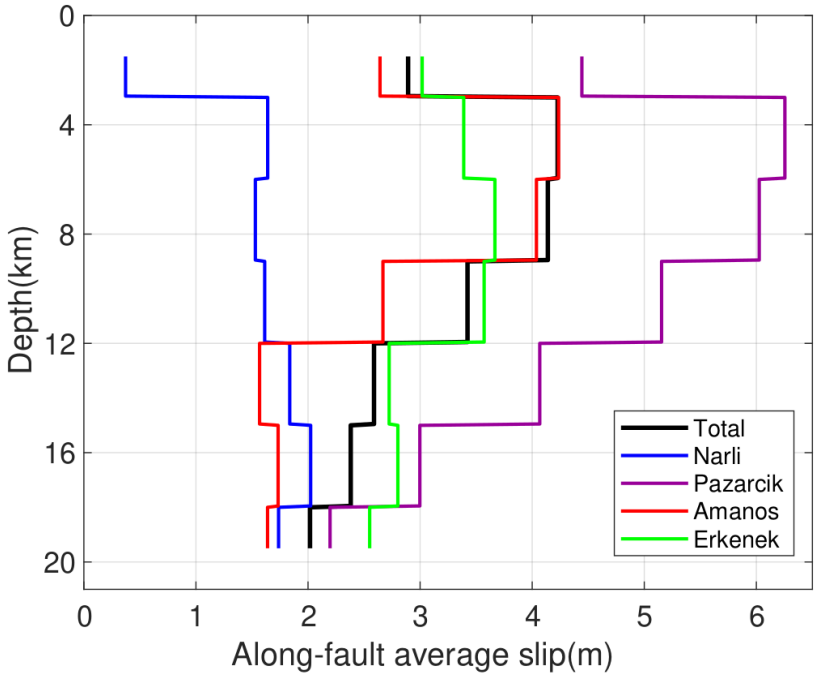

Supplementary Figure 14. The along-fault averaged slip as a function of depth for all fault segments and the entire slip model.

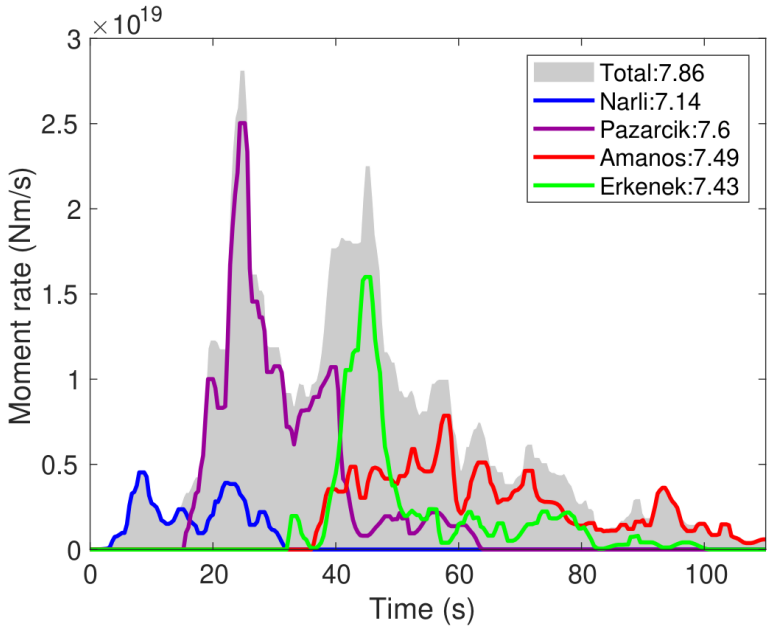

Supplementary Figure 15. Moment rate functions. The gray-shaded area represents the whole rupture process. The color lines indicate the moment rate function on each fault segment. The moment magnitude on each segment is shown in the legend.

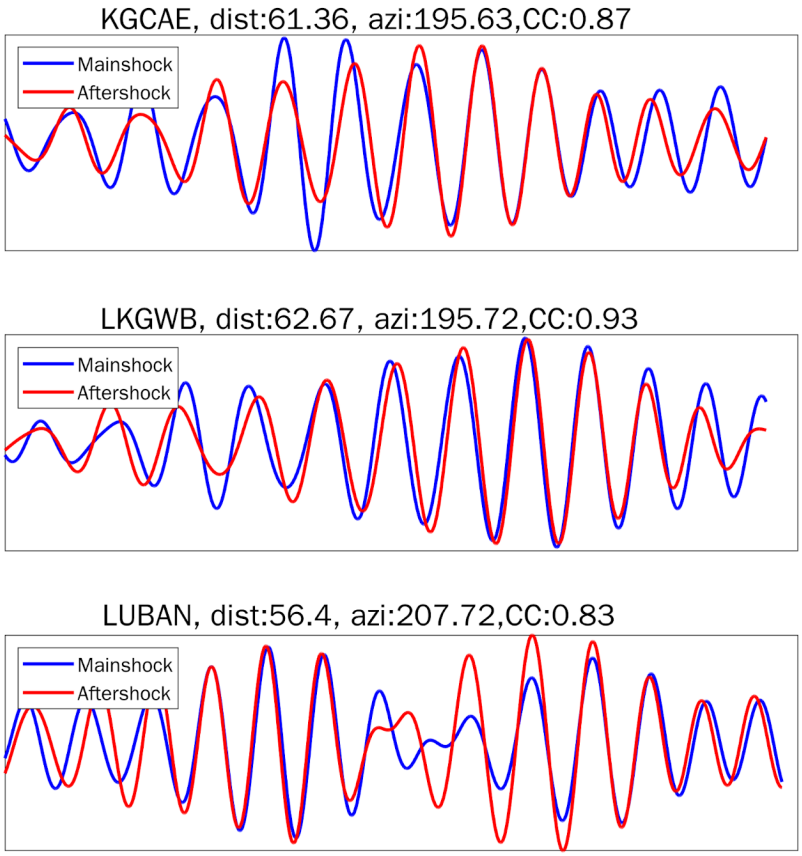

Supplementary Figure 16. The Rayleigh wave vertical displacement seismograms of mainshock (blue) and aftershock (red) in the 15–25 s period range recorded at stations located in the direction of south rupture. Station name, azimuths in degree (azi), hypocentral distance in degree (dist), and correlation coefficient (CC) are shown in the titles.

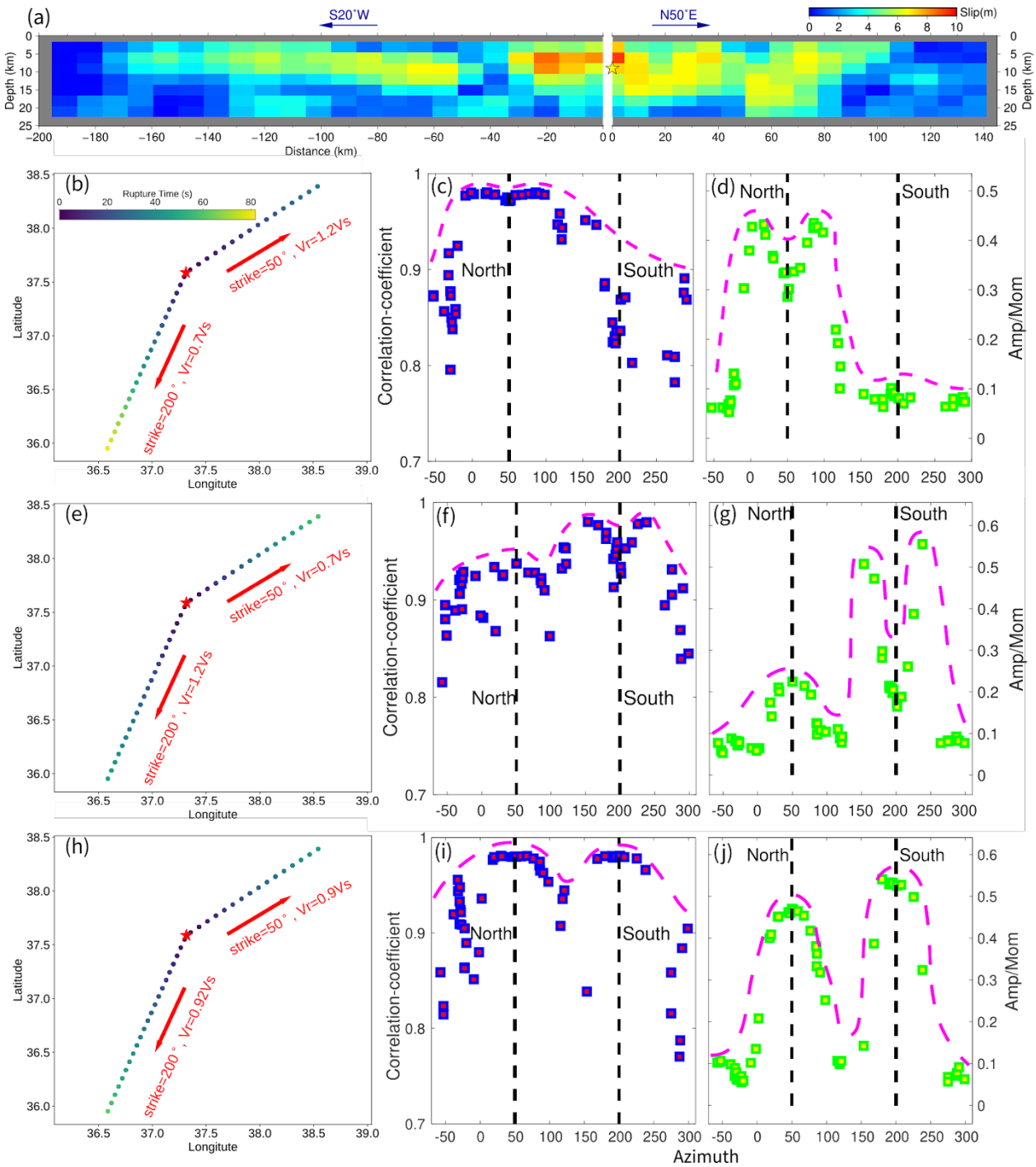

Supplementary Figure 17. Mach wave synthetic test for bilateral ruptures. (a) The bilateral slip model. Blue arrows and words indicate the strike direction of two branches. The yellow star denotes the hypocenter. (b) Input bilateral rupture propagation. The northeast speed is supershear (1.2*Vs), and the southwest rupture is subshear (0.7*Vs). (c) Cross-correlation Coefficients (CCs) distribution as a function of azimuth. The pink dash curve indicates the envelope delineating the distribution pattern of CCs. (d) Amplitude ratio over the seismic moment ratio. Amplitude ratio = amplitude[mainshock waveform]/amplitude[aftershock waveform]. Moment

ratio = moment of the mainshock / moment of the aftershock. (e-g) The same as (b-d) but for subshear northeast rupture (0.7*Vs) and supershear southwest rupture (1.2*Vs). (h-j) The same as (b-d) but for rupture speeds resolved in this study (northeast ~0.9Vs, southwest ~0.92Vs).

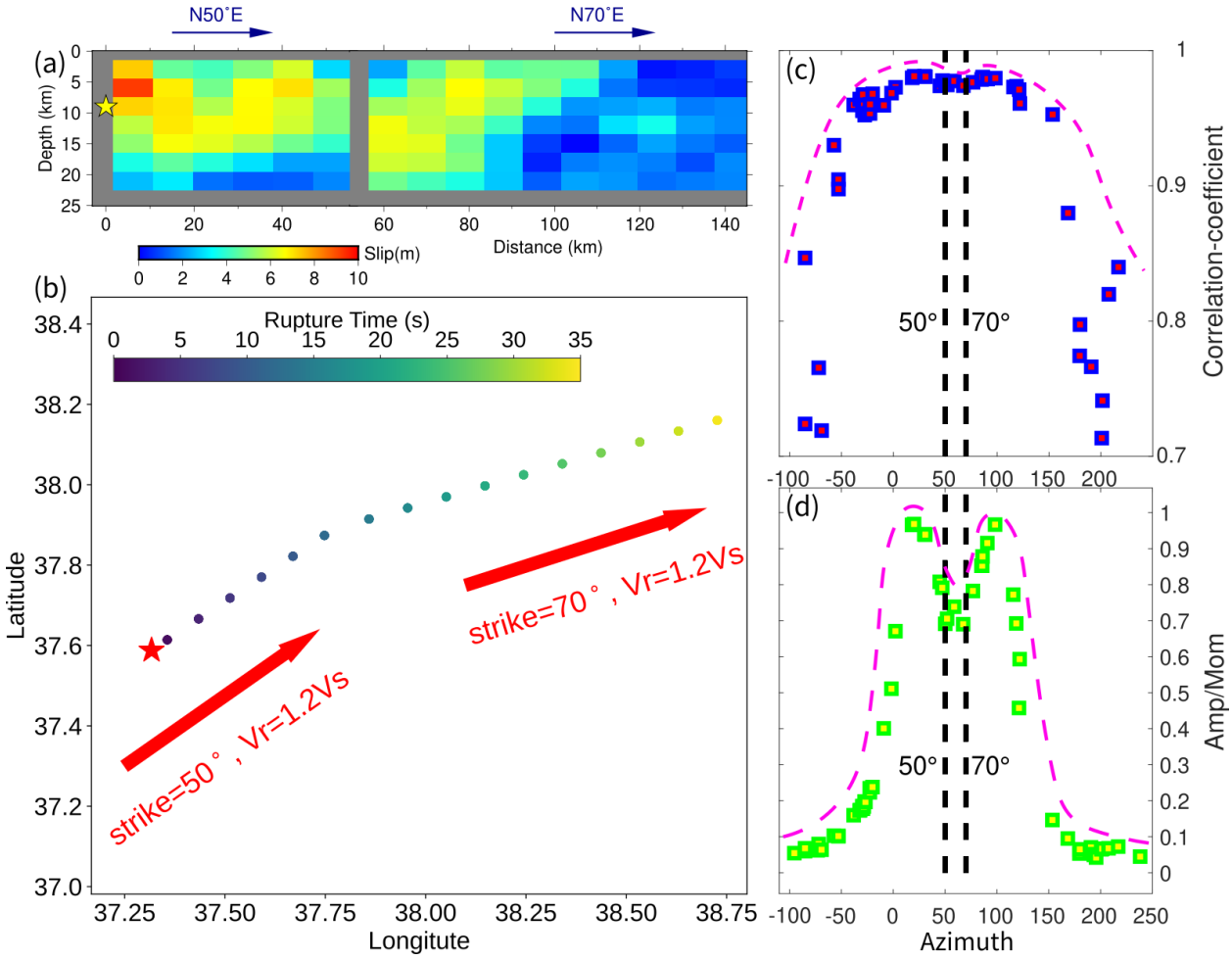

Supplementary Figure 18. Mach wave synthetic test for the kinked rupture. (a) The kinked slip model. Blue arrows and words indicate the strike direction of two segments. The yellow star denotes the hypocenter. (b) Input rupture propagation. Both segments are supershear (1.2*Vs) but segment 1 has a strike of 50° and segment 2 has a strike of 70°. (c) Cross-correlation Coefficients (CCs) distribution as a function of azimuth. The pink dash curve indicates the envelope delineating the distribution pattern of CCs. (d) Amplitude ratio over the seismic moment ratio.

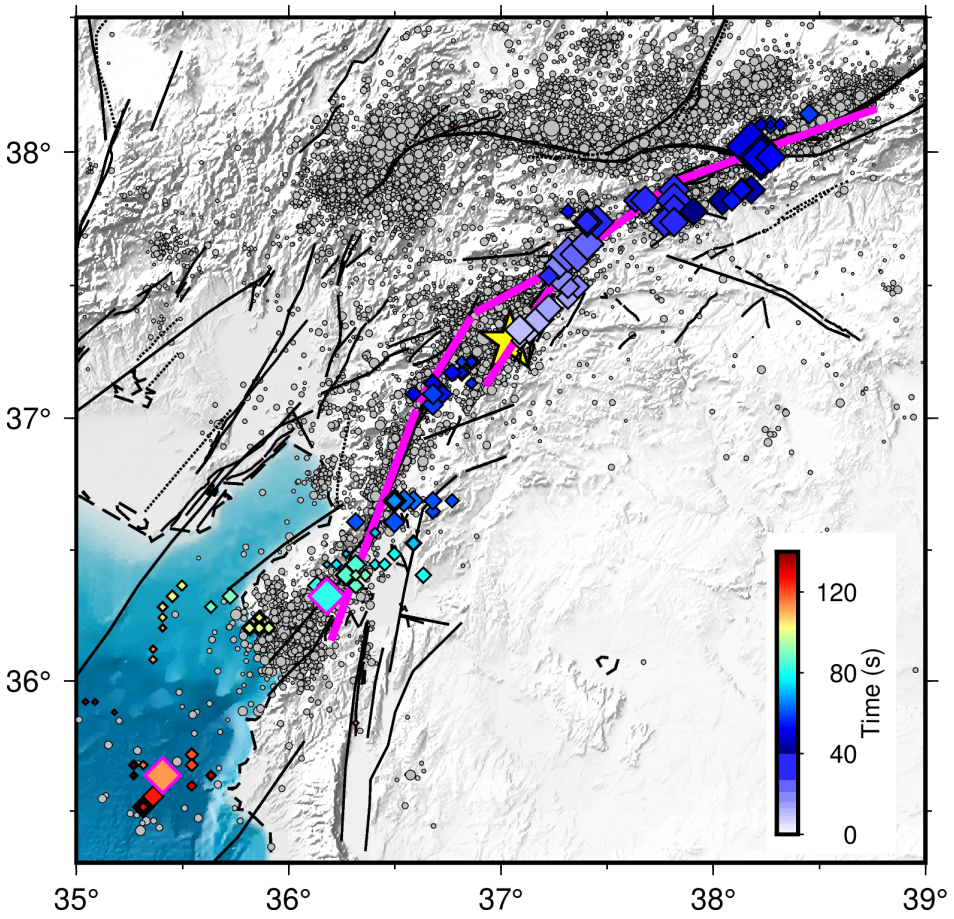

Supplementary Figure 19. Two High-Freq radiators used for S wave travel time calculation. The cyan diamond with magenta edge is the last radiator on the Amanos segment, and the red diamond with magenta edge is the first radiator for the triggered offshore event.

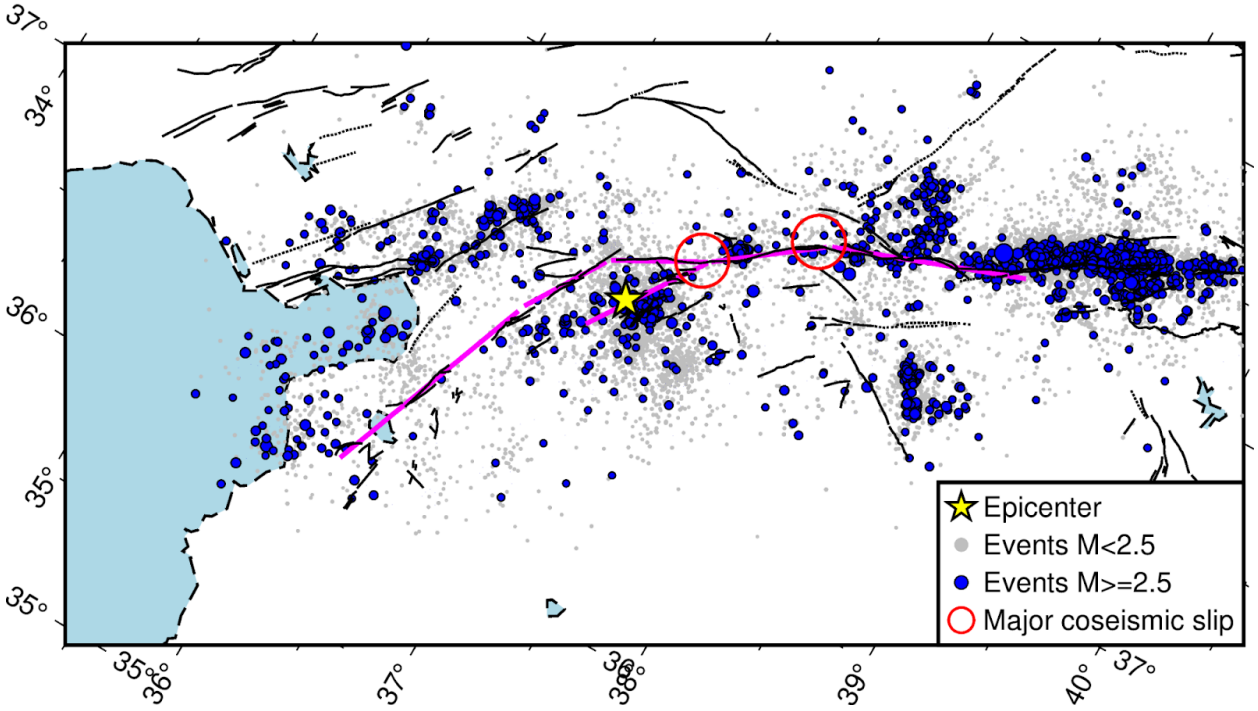

Supplementary Figure 20. Consistency between seismicity voids and major coseismic slip asperities. The red circles highlight the regions where large coseismic slip and seismicity voids appear simultaneously. The seismicities occurred between 2007 to 2020 and are from Güvercin et al.[11].

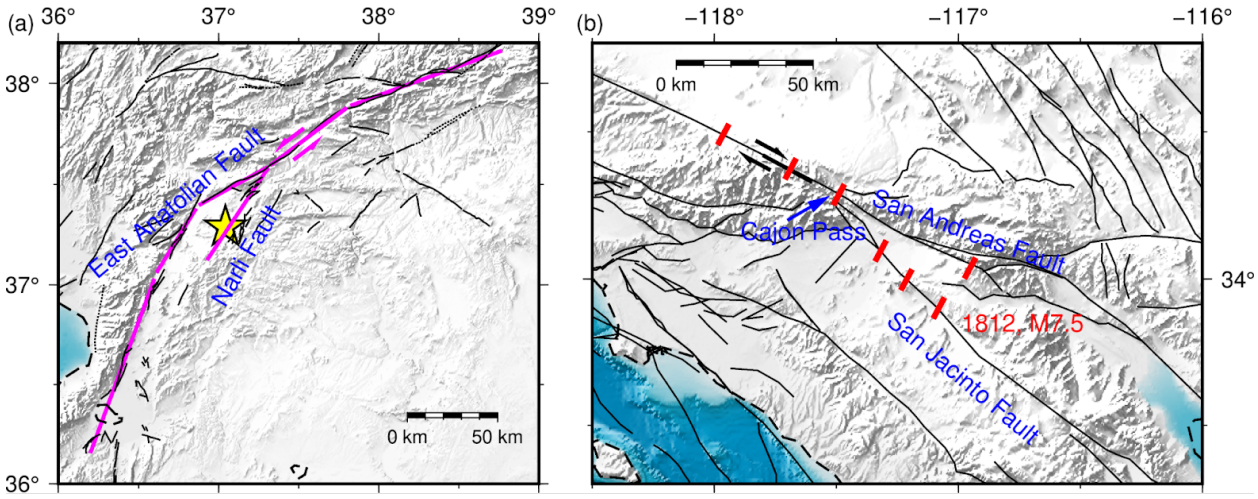

Supplementary Figure 21. Map of the East Anatolian Fault and San Andreas Fault systems. The magenta arrows in (a) and black arrows in (b) show fault motions. The yellow star in (a) denotes the epicenter of the 2023 Mw7.8 event. Red bars in (b) represent the paleoseismic sites of the early 1800 earthquake, adapted from Lozos[14].

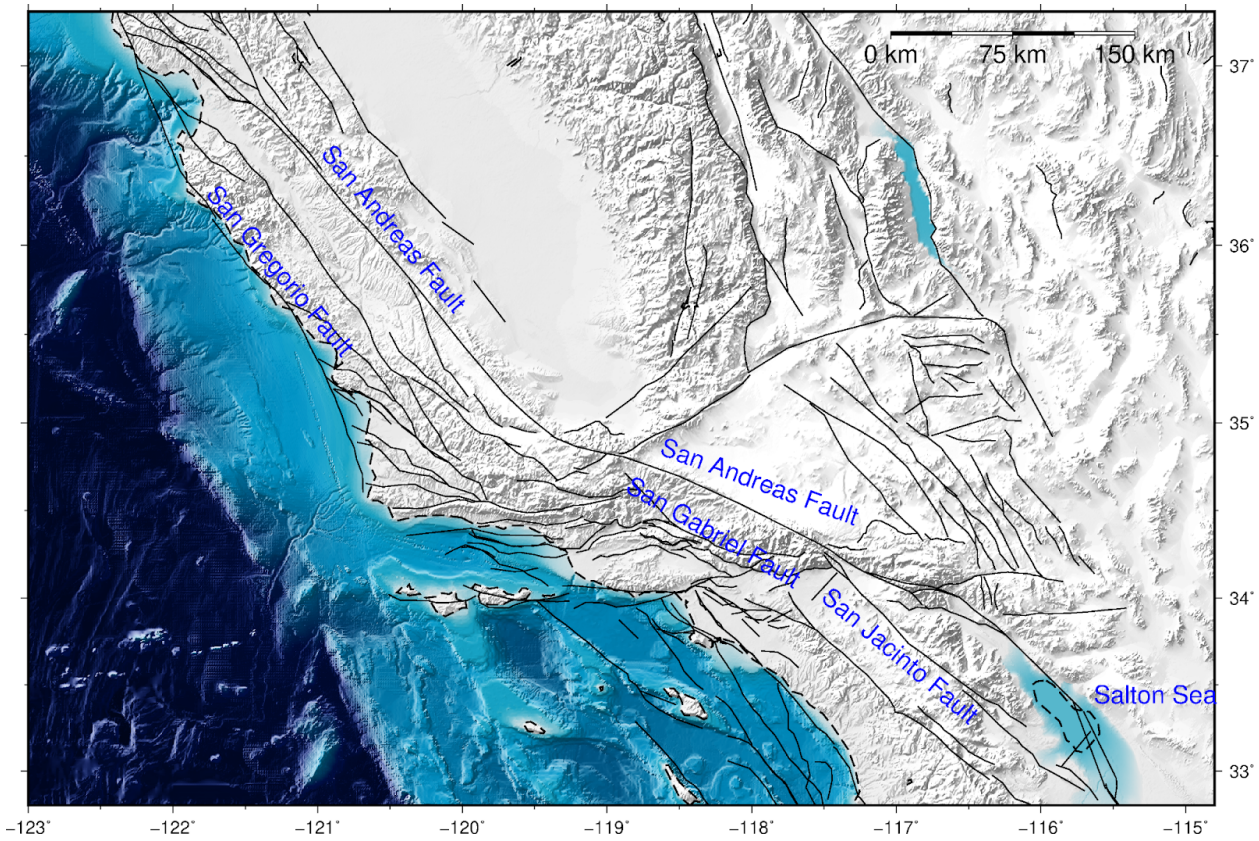

Supplementary Figure 22. The San Jacinto Fault, San Gabriel Fault, San Gregorio Fault, and San Andreas Fault.

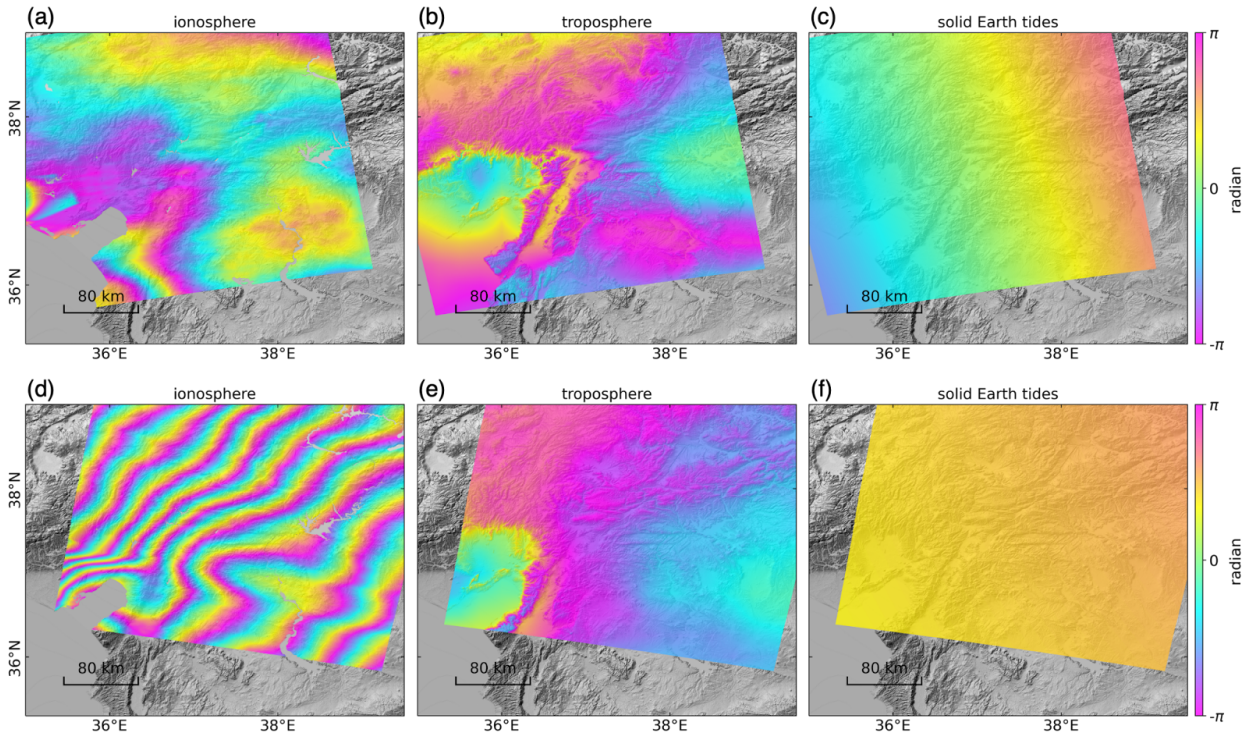

Supplementary Figure 23. Phase corrections for ALOS-2 InSAR displacement. (a-c) Estimated ionospheric delay using range split-spectrum, tropospheric delay using ERA5 global atmospheric model, and solid Earth tides following the 2010 IERS convention, respectively, for the ascending track 184 at 00:30 am local time. (d-f) Same as (a-c) but for the descending track 077 at 12:30 pm local time.

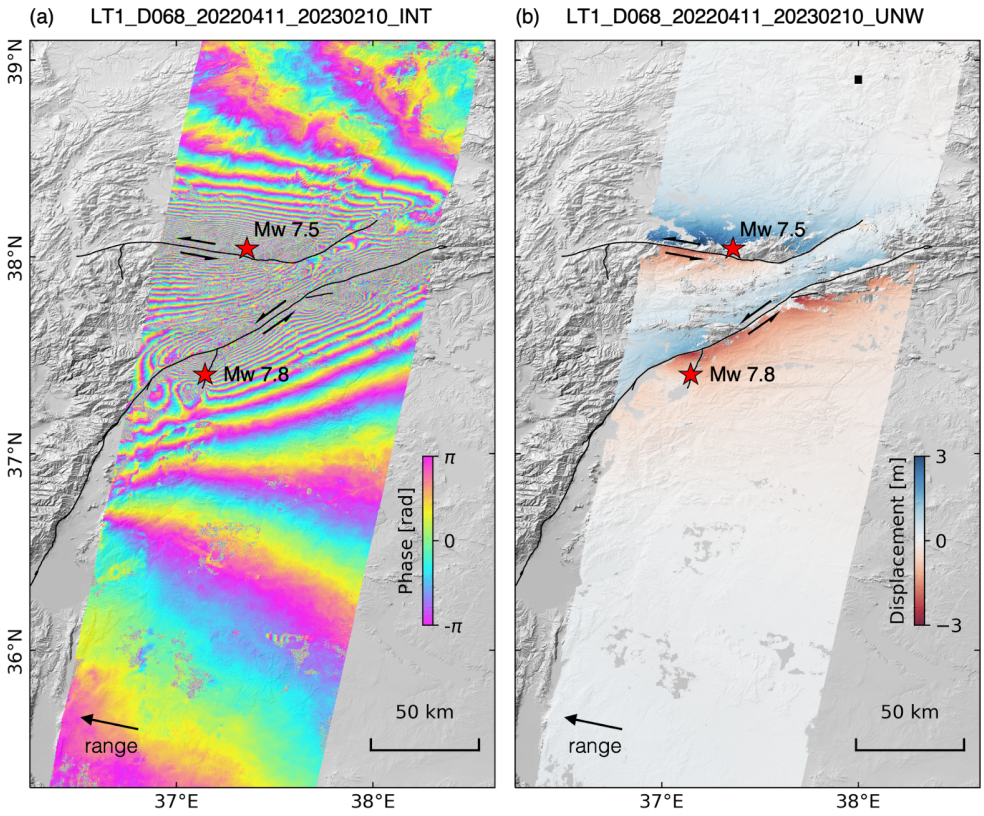

Supplementary Figure 24. LuTan-1 interferograms (a) before and (b) after phase unwrapping. Black square in (b): reference point. Red stars denote the epicenter of the two earthquakes.

Supplementary References

1. Rosakis, A., Abdelmeguid, M., & Elbanna, A. Evidence of Early Supershear Transition in the Mw 7.8 Kahramanmaras Earthquake From Near-Field Records. arXiv preprint. arXiv:2302.07214 (2023).

2. Melgar, D. et al. Sub- and super-shear ruptures during the 2023 Mw 7.8 and Mw 7.6 earthquake doublet in SE Türkiye. Seismica, 2, 3 (2023).

3. Okuwaki, R., Yuji, Y., Taymaz, T., & Hicks, S. P. Multi-scale rupture growth with alternating directions in a complex fault network during the 2023 south-eastern Türkiye and Syria earthquake doublet. eartharxiv.org (2023). https://doi.org/10.31223/X5RD4W.

4. Yao. S, & Yang. H. Rupture phase in near-fault records of the 2023 Turkey Mw 7.8 earthquake. EarthArXiv (2023), https://doi.org/10.31223/X51662.

5. Delouis, B., van den Ende, M., & Ampuero, J.-P. Kinematic rupture model of the February 6th 2023 Mw 7.8 Turkey earthquake from a large set of near-source strong motion records combined by GNSS

offsets reveals intermittent supershear rupture. Authorea (2023). https://doi.org/10.22541/essoar.168286647.71550161/v1.

6. Abdelmeguid, M. et al. Revealing The dynamics of the Feb 6th 2023 M7.8 Kahramanmaracs/Pazarcik Earthquake: near-field records and dynamic rupture modeling, arXiv (2023). https://doi.org/10.48550/arXiv.2305.01825.

7. Mai, P. M. et al. The Destructive Earthquake Doublet of 6 February 2023 in South-Central Türkiye and Northwestern Syria: Initial Observations and Analyses. The Seismic Record, 3(2), 105–115 (2023).

8. Petersen, G. M. et al. The 2023 Southeast Türkiye Seismic Sequence: Rupture of a Complex Fault Network. The Seismic Record. 3 (2), 134–143 (2023).

9. Wang. Z. et al. Dynamic rupture process of the Mw 7.8 Kahramanmaraş earthquake (SE Türkiye): Variable rupture speed and implications for seismic hazard. Authorea (2023). https://doi.org/10.22541/essoar.168614604.40356164/v1

10. Duman T.Y. & Emre Ö. The East Anatolian Fault: geometry, segmentation and jog characteristics, *Geol. Soc. Spec. Publ.*, **372**, 495–529 (2013).

11. Güvercin, S. E., Karabulut, H., Konca, A. Ö., Doğan, U., & Ergintav, S. Active seismotectonics of the East Anatolian Fault. *Geophys. J. Int.* **230**, 1, 50–69 (2022).

12. Ambraseys, N. & Jackson, J. Faulting associated with historical and recent earthquakes in the Eastern Mediterranean region, *Geophys. J. Int.* **133**, 2, 390–406 (1998).

13. Palutoglt. M. & Sasmaz. A. 29 November 1795 Kahramanmaras Earthquake, Southern Turkey. *Bulletin of the Mineral Research and Exploration*. **155**, 155, 187 - 202 (2017).

14. Lozos, J. C. A case for historic joint rupture of the San Andreas and San Jacinto faults. *Science Advances*, **2**, 3, e1500621 (2016).